Compaction and sedimentary basin analysis on Mars

Leila R. Gabasova [*,1], Edwin S. Kite

Hinds Building, 5734 S Ellis Ave, University of Chicago, Chicago, IL 60637, USA

A B S T R A C T

Many of the sedimentary basins of Mars show patterns of faults and off-horizontal layers that, if correctly understood, could serve as a key to basin history. Sediment compaction is a possible cause of these patterns. We quantified the possible role of differential sediment compaction for two Martian sedimentary basins: the sediment fill of Gunjur crater (which shows concentric graben), and the sediment fill of Gale crater (which shows outward-dipping layers). We assume that basement topography for these craters is similar to the present-day topography of complex craters that lack sediment infill. For Gunjur, we find that differential compaction produces maximum strains consistent with the locations of observed graben. For Gale, we were able to approximately reproduce the observed layer orientations measured from orbiter image-based digital terrain models, but only with a >3 km-thick donut-shaped past overburden. It is not immediately obvious what geologic processes could produce this shape.

1. Introduction

Under pressure, sediment grains rearrange, fragment, and dissolve at grain contacts. When the pressure is due to geologic overburden, the resulting reduction of porosity is referred to as compaction. Compaction converts sediment to rock, drives basin-scale tectonics, expels pore fluids, and deflects layers. Recognizing compaction from Mars orbit may allow ancient sediment-filled basins to be distinguished from ancient lava-filled basins since compaction is more likely to be observed in highly porous sedimentary rocks than in incompressible volcanic rocks. Once a sedimentary basin has been recognized, accounting for compaction is fundamental to reconstructing the sedimentary history (Allen and Allen, 2005). Compaction-driven flow can drive diagenesis, compaction anomalies may indicate the presence of past overburden (i.e., erosional unconformities), and compaction-driven subsidence can cause faults (Castle and Yerkes, 1976). Finally, differential compaction can alter stratal geometries. Because clues to past depositional processes, paleoclimate, and water-level change within sedimentary basins can be obtained from stratal geometries, quantifying the dip due to differential compaction (in basins where stratal geometries are well exposed, such as Gale) is important (Grotzinger et al., 2015).

Despite its importance, there has been relatively little work on compaction on Mars, in part because the data used to study basin compaction on Earth (e.g. core data) do not yet exist for Mars.

Buczkowski and Cooke (2004) interpret double-ring graben in Utopia as the fingerprint of differential compaction (and thus sedimentary infill). Lefort et al. (2012, 2015) argue that differential compaction in Aeolis-Zephyria contributes to channel slope reversal. In this contribution, we first show how compaction works for idealized container (rift or crater) geometries (§2). We then apply this understanding to two sedimentary basins on Mars: the infill of Gunjur (27 km diameter, 0.2°S, 146.7°E) (§3), and the infill of Gale (154 km diameter, 5.4S°S, 137.8°E) (§4). This analysis cannot yet be generalized to all sedimentary basins on Mars, lacking measurements such as grain size and porosity, but knowledge of the specific geologic conditions in these two basins allows us to propose analogous terrestrial properties for the sediments. We discuss implications in §5 and conclude in §6.

2. Idealized calculations

To gain intuition for the effects of compaction, we first calculate compaction for idealized Mars sedimentary-basin geometries. We make the following assumptions:

1. Present-day porosity loss reflects maximum pressure, not present-day pressure – i.e. hysteresis following unloading is minimal (Wangen, 2010).

2. The basal layer underlying the sedimentary infill is rigid and non-compactible (either because it is low-porosity, poorly compressible igneous rock, or because it has previously been compacted).

3. Compaction is parametrized by an exponential decay of porosity with depth, with a decay constant that depends on gravity and on the lithology of the material being compacted (Athy, 1930; Baldwin and Butler, 1985).

4. Compaction is fast relative to the rate of sedimentation, i.e. pore-filling fluids can migrate upwards faster than the rate of loading, and compaction equilibrium is maintained within the basin. Compaction is thus not limited by rock permeability.

5. Compaction is produced mainly by grain rearrangement; we neglect the compression of individual grains, which is small.

6. The Mars elastic lithosphere thickness at the time of loading is comparable to or greater than the basin width, and so flexure is small and can be neglected.

For calculations involving layer deflections, we make the additional assumption, as its being incorrect would have no or minimal effect on the cases studied here:

7. Layers are initially horizontal.

We first consider the compaction of a single column. Its porosity will decay with depth exponentially as follows:

$$\phi = \phi_0 \times e^{-cz} \tag{1}$$

Here, ϕ represents porosity, z the depth and c an empirical constant which must be adjusted for Martian gravity: $c_{Mars} = \frac{c_{Earth}}{9.81} \times 3.71$. Values for ϕ and c for different consolidated materials are given in Table 1. For the remainder of this paper, the 2009 values will be used.

As per assumption 5 above, the total sediment grain volume remains constant, which means the column volume depends only on its porosity. As the column is assumed to be constrained on all sides, its horizontal section also does not change; the decrease in column volume is thus reflected only in its height.

To determine the difference in height due to compaction, we integrate Eq. (1) over z as shown in Eq. (2), obtaining Eq. (3). For ease of calculation, we express z_0, the column height at uniform porosity, as a function of z, the fully compacted height. If z need be obtained, we use simple numeric iteration to converge towards a value which would produce a particular z_0.

$$\int_{\phi_0}^{\phi} \frac{\phi}{\phi_0} = \int_{z_0}^{z} e^{-cz} \tag{2}$$

$$z_0 = \frac{z + \frac{\phi_0}{c} \times (e^{-cz} - 1)}{1 - \phi_0} \tag{3}$$

We now consider two adjacent sediment columns in a basin with an uneven floor. The sediment infill is initially deposited in horizontal layers already compacted under their own weight as per assumption 4. As more layers are added, they produce further compaction in the layers below. However, due to the uneven floor the column heights are different, so this results in two different degrees of compaction. A given sediment layer is

now no longer at the same height in the two adjacent columns: it is tilted, or dipped. This process is illustrated in Fig. 1. The analytic expression for this tilt, or dip, T, expressed in degrees, is as follows, with dx representing the distance between columns and dz the difference in final layer elevation:

$$T = \tan^{-1}\left(\frac{dz}{dx}\right) \tag{4}$$

We calculate dz, the difference between layer height at deposition, and its height after compaction due to overburden, according to Eq. (3).

To quantify the effect of compaction on dip, we study the following idealized cases:

1. A **simple crater** with diameter $D = 10$ km and depth $d \approx 1320$ m (scaling parameters for simple craters used from Tornabene et al. (2013): $d = 0.267D^{0.68}$)

2. A **complex crater** with a **central peak**, with diameter $D = 40$ km, depth $d \approx 2430$ m (scaling parameters for complex craters used from Tornabene et al. (2013): $d = 0.357D^{0.52}$) and central peak height $h_p \approx 1250$ m.

3. A **complex crater** with a **peak ring**, with diameter $D = 200$ km, depth $d \approx 5610$ m (scaling parameters same as for central-peak crater) and a peak ring with height $h_p \approx 2870$ m and diameter $D_p = 30$ km.

Figs. 2–4 show cross-sections and maps of sediment thickness and horizontal dip for these three cases respectively, assuming the crater is uniformly filled with sandstone. The maps show: (i) the **original** thickness of the sediment infill as we find it, after compaction has occurred; (ii) the **decompacted** thickness after we reverse the effect of compaction and obtain an infill of uniform porosity; (iii) the **difference** between the first two maps; (iv) the **maximum dip**, which shows for each column the maximal amount of dip over all depths (sampled at whole percentage values of depth); and (v) the horizontal strain. The horizontal strain is calculated using the second derivative of the dip and the sediment thickness according to the equation derived by Lee and Shen (1969) (see Eq. (5)). We assume faulting will initiate where the horizontal strain is maximal (Jachens and Holzer, 1982; Panda et al., 2015). Therefore the most likely distribution of faults can be traced using the strain map, and faulting can initiate for values of strain as low as 0.02% although it is more probable for values above 1% (Jachens and Holzer, 1982).

$$\varepsilon = \frac{2}{3}H\nabla T \text{ where } \nabla T \text{ is dip derivative } (\text{in } m^{-1}), \tag{5}$$
$$\text{and } H \text{ is sediment thickness (in m)}$$

In the simple crater case (Fig. 2), the compaction degree increases smoothly from rim to crater center. The dip is maximal at approximately 0.6 crater radii and flattens out towards the crater center, with the largest horizontal strain being around the crater rim and at ~ 0.3 radii, where the dip flattens. In this case, we might expect concentric faulting around the rim and at ~ 0.3 radii.

In the case of the complex crater with a central peak (Fig. 3), the surface profile from the peak to the rim takes on a bowl-like shape. The compaction is maximal between 0.3 and 0.5 radii; there is a strong inward dip close to the rim, no dip in the maximal compaction region and a pronounced outward dip encircling the central peak. The horizontal strain is greatest around the crater rim and around the central peak; these are the potential faulting locations.

Finally, the peak-ring crater (Fig. 4) combines the two previous cases. We observe significant inward dipping around the rim and around the inner edge of the peak ring and matching outward dipping around its outer edge. The horizontal strain is most pronounced, and probability of faulting is highest, close the rim as well as at the top of the peak ring.

As the crater diameter increases, so does the infill depth, which in turn increases the horizontal strain. In our three examples, we go from

Table 1
Empirical values of ϕ and c for sandstone and shale, adjusted to Martian gravity, taken from Hantschel and Kauerauf (2009), with values from Sclater and Christie (1980) for comparison to illustrate the uncertainty in basin-scale compaction parameters.

Lithology	Hantschel and Kauerauf (2009)		Sclater and Christie (1980)	
	Sandstone	Shale	Sandstone	Shale
ϕ_0	0.41	0.70	0.49	0.63
c_{Mars} (km^{-1})	0.117	0.314	0.102	0.193
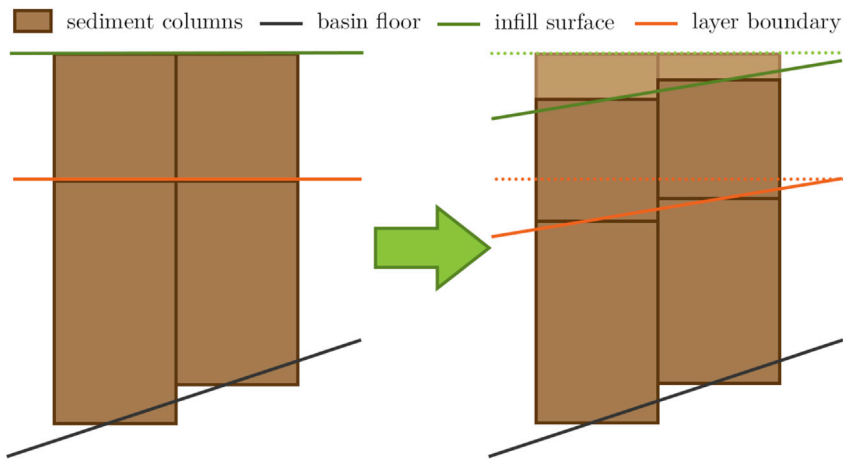
Fig. 1. A schematic showing the differential compaction of two adjacent columns of different height after infill is added. The new infill surface and the inner layer boundary (the old infill surface) are initially horizontal, but become tilted due to the columns compacting differently.

~0.01% maximal strain for the simple crater case to 0.045% for the peak ring crater, which suggests that faulting potential is higher for deeper infill.

3. Basin analysis at Gunjur: evidence for compaction-driven faults

3.1. Gunjur crater's faults in context

Gunjur crater is a partly infilled complex crater 600 km ENE of Gale crater (Kite et al., 2015b). Gunjur formed in a lobe of Medusae Fossae "Formation" materials that are mapped as Hesperian (Tanaka et al., 2014). Gunjur's ejecta appear bright in THEMIS IR nighttime images. There are at least 9 craters with a diameter >1 km on Gunjur's ejecta, indicating a pre-Amazonian age for the crater. Alluvial-fan activity at Gunjur likely postdates Late Noachian or Early Hesperian river deposits in the trough immediately east of the Gunjur-hosting lobe (Williams et al., 2013; Kite et al., 2015a).

Gunjur has a large alcove to the W and smaller alcoves to the N and S that are linked to the smooth floor by sinuous ridges. We interpret these ridges as inverted channels corresponding to sediment transport pathways (Burr et al., 2009; Harrison et al., 2013). The total volume of the alcoves can be calculated by subtracting present-day topography from a surface calculated by constructing, via natural neighbor interpolation, a smooth spline across the present-day rim (e.g., Palucis et al., 2016). Using this procedure, the total volume of the alcoves is 149.2 km^3. The alcove area is 561 km^2, so the mean erosion is 266 m.

The volume of sediment infilling Gunjur crater can be calculated by subtracting the azimuthally-averaged floor elevation of a similarly-sized crater from the present-day topography (e.g. Grant et al., 2016). This floor elevation profile is obtained by making 120 radial profiles of each crater (spaced out by 3°), and taking the arithmetic mean of these profiles for each given distance from the crater center. Using this procedure, the volume of sediment infilling Gunjur (excluding late-stage yardang-forming materials) is 145.7 km^3. The volume agreement between the alcove volume and the infill volume implies that the Gunjur basin fill was transported by a downslope movement, most likely fluvial sediment transport or debris-flow erosion (both of which require surface liquid water). Supporting this inference, paleochannels embedded within early-stage Gunjur basin fill are visible in HiRISE images extending from the western rim all the way to the central peak (see Fig. 6). Paleochannel alignment always indicates sediment transport from rim to crater floor, never from central peak to crater floor.

Subsequent to basin infill, alluvial fans formed. We distinguish the fan-formation event from the earlier sediment deposit events which form the infill because of the fans' pronounced conical shapes, absent in the earlier deposits, and slopes which are steeper than the layer dips of the basin infill. Alluvial fans represent a relatively small-volume (4.88 km^3 sediment, or 2442 km^3 water assuming a 500:1 water:sediment ratio), relatively late-stage and polyphase wet event. Two steep-fronted flat-topped depositional features, which may be deltas, are also seen.

Gunjur's floor (both near the edge of the crater, and around the central peak) shows circumferential graben. Circumferential extensional faulting and fissuring is expected for differential subsidence/compaction (Lee and Shen, 1969; Castle and Yerkes, 1976; Odonne et al., 1999). Relations between graben and alluvial fans constrain the timing of alluvial fan activity: the most voluminous alluvial fan is crosscut by graben, but the less voluminous alluvial fans overlie the graben (the relevant fans are shaded in green on Fig. 5). Because the graben are in the same state of erosion and appear to represent a single event, this implies at least two phases of runoff. Multiple phases of runoff are also indicated at Gale, at Holden, and at SW Melas Chasma (Palucis, 2014; Grant et al., 2008a; Williams and Weitz, 2014). The last major (≫ 1 m thickness) depositional event at Gunjur was the formation of a light-toned layered unit that superposes the alluvial fans and the graben: the rhythmic bedding suggests its sedimentary origin (Lewis and Aharonson, 2014). This unit has been eroded to form yardangs.

Gunjur's floor is almost flat, except for the relatively steeply-sloping alluvial fans. This slope break is further evidence that most of the infilling is lake deposits or deltaic deposits, with only a volumetrically minor late-stage contribution by steeply-sloping alluvial fans. This is also the sequence suggested for the evolution of Gale crater (Grotzinger et al., 2015).

The overall pattern of concentric faults at Gunjur is consistent with that expected for differential compaction. Other common causes of concentric graben formation are subsidence due to volcanic loading (Cailleau et al., 2003; Branney, 1995), which is not applicable to the case of a sedimentary basin, or sublimation of massive ice from the crater interior (Levy et al., 2013), which cannot be ruled out but is also not supported by evidence (i.e. sublimation pits).

Significant differential compaction is suggested by the remarkably large width and depth of the graben: Fig. 7 shows one of the larger graben in Gunjur having a width of ~100 m and a depth of up to 10 m. This large width and depth could be caused by high initial sediment porosity (we assume mudstone-type sediment as observed in other lacustrine formations (Grotzinger et al., 2015), with initial porosity similar to shale as in Table 1), by a sharp horizontal contrast in grain size (e.g., sharp and systematic gravel → silt transition moving in from the edge of the crater toward the center), or by now-vanished additional overburden. Now-vanished overburden implies a deposition-erosion cycle (Kite et al., 2016). Evidence for a recent deposition-erosion cycle exists at Gunjur: a mostly-eroded layered sedimentary unit that formed yardangs. Remarkably, although the yardangs crosscut the faults, they are not themselves faulted. This suggests that the deposition of the yardang-forming unit
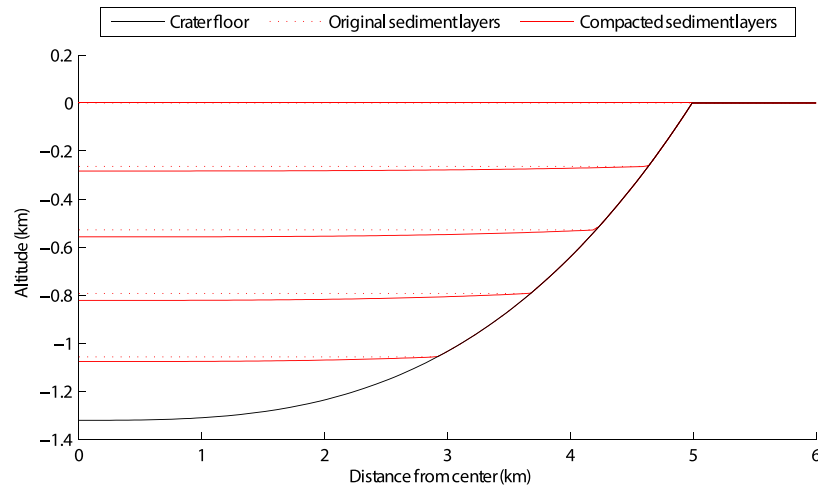
(a) Crater cross-section
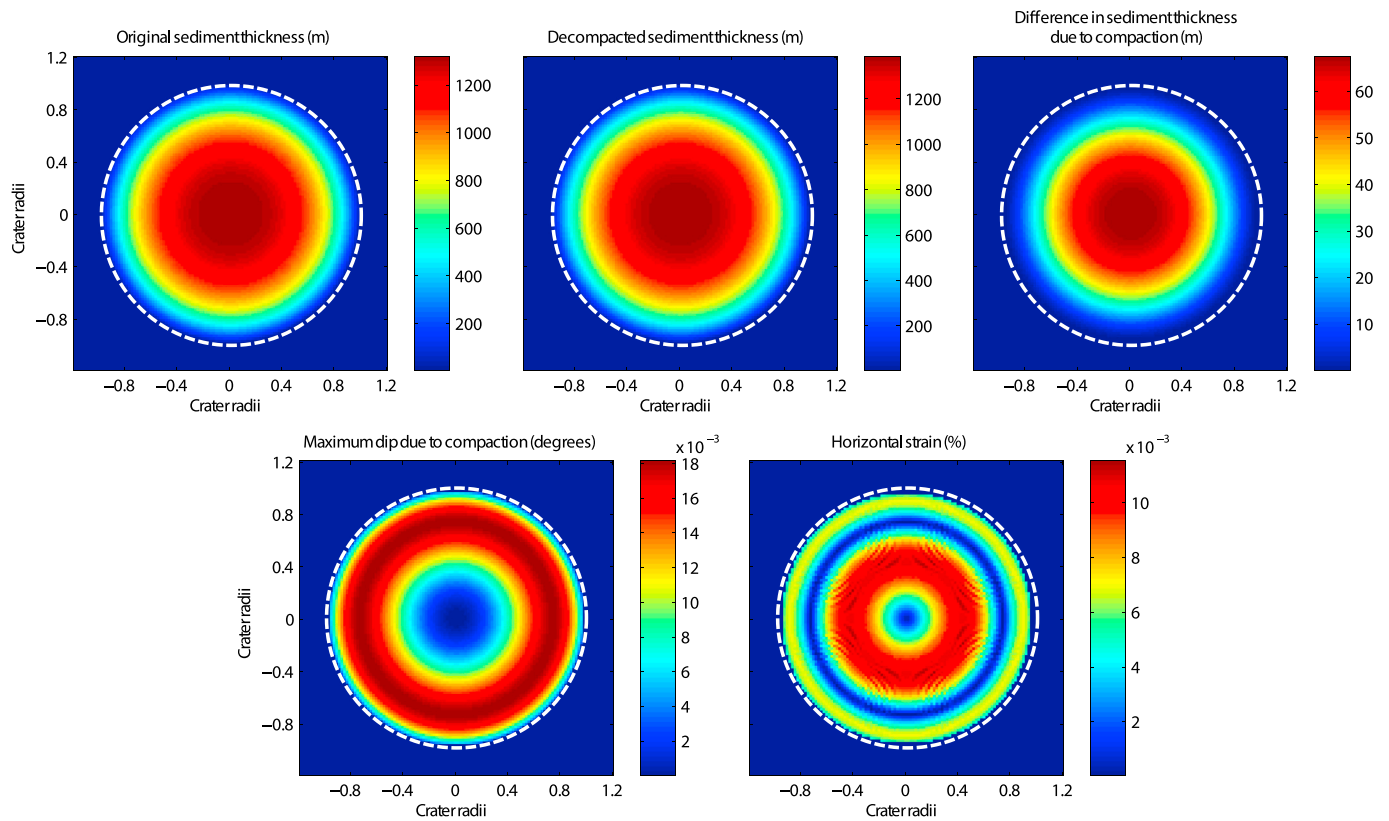
(b) Crater maps (for 100% infill), with crater boundary marked with dotted white line
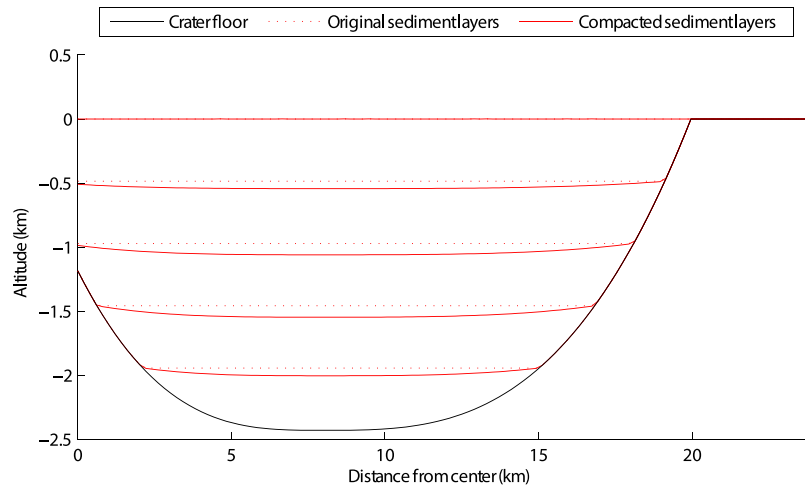
Fig. 2. Effect of sediment compaction modeled for an idealized simple crater. Note that each map has its own individual colorbar, showing depth in m for sediment thickness, degrees for dip, and % for horizontal strain.

postdates the faults, and that the pressure of the yardang-forming layer (>100 m thick) did not cause further compaction. In turn, this suggests that the faulting was driven by a now-vanished overburden layer, and that layer was thicker than 100 m. This corresponds to between 1 and 3 My of accumulation if using a sedimentation rate of 30–100 μm/yr as given by Lewis and Aharonson (2014) for yardang-forming light-toned sedimentary rocks. Alternatively, the graben could have formed by self-compaction of sediment infill that was at least as compactible as shale (see Table 1).

3.2. Forward modeling differential-compaction strain at Gunjur

In the following section, we calculate the differential compaction expected for different infilling scenarios at Gunjur. We then use the x-y derivative of these differential-compaction maps to calculate the relative amplitude of differential-compaction strain. Our calculations are for 1-D compaction, but the pattern of differential compaction should be very similar for 3-D compaction.

Our data for Gunjur is in the form of 120 radial topographic profiles, with an average of one measurement per 270 m. To determine the sediment depth at each point, we subtract the surface altitude measure-

(a) Crater cross-section
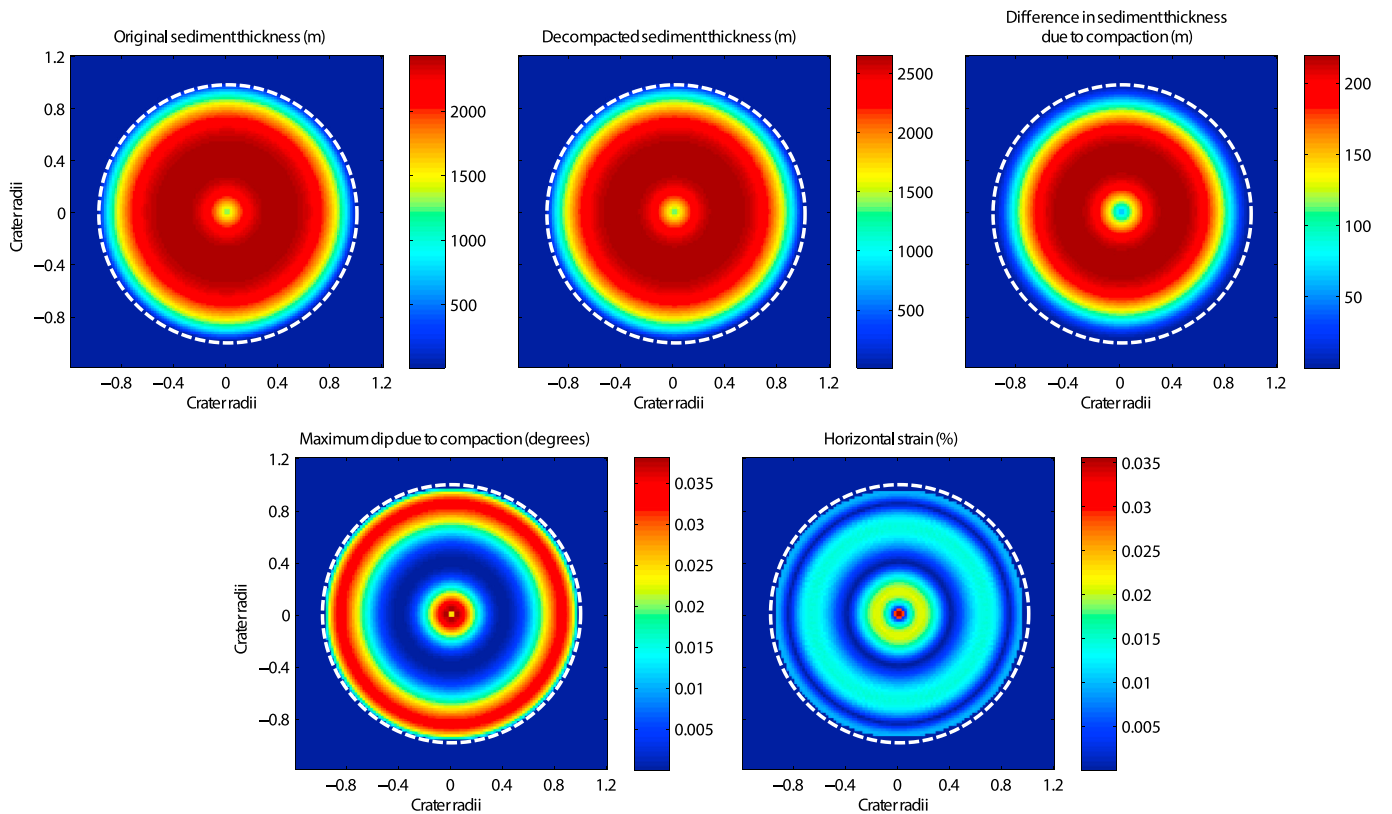
(b) Crater maps (for 100% infill), with crater boundary marked with dotted white line
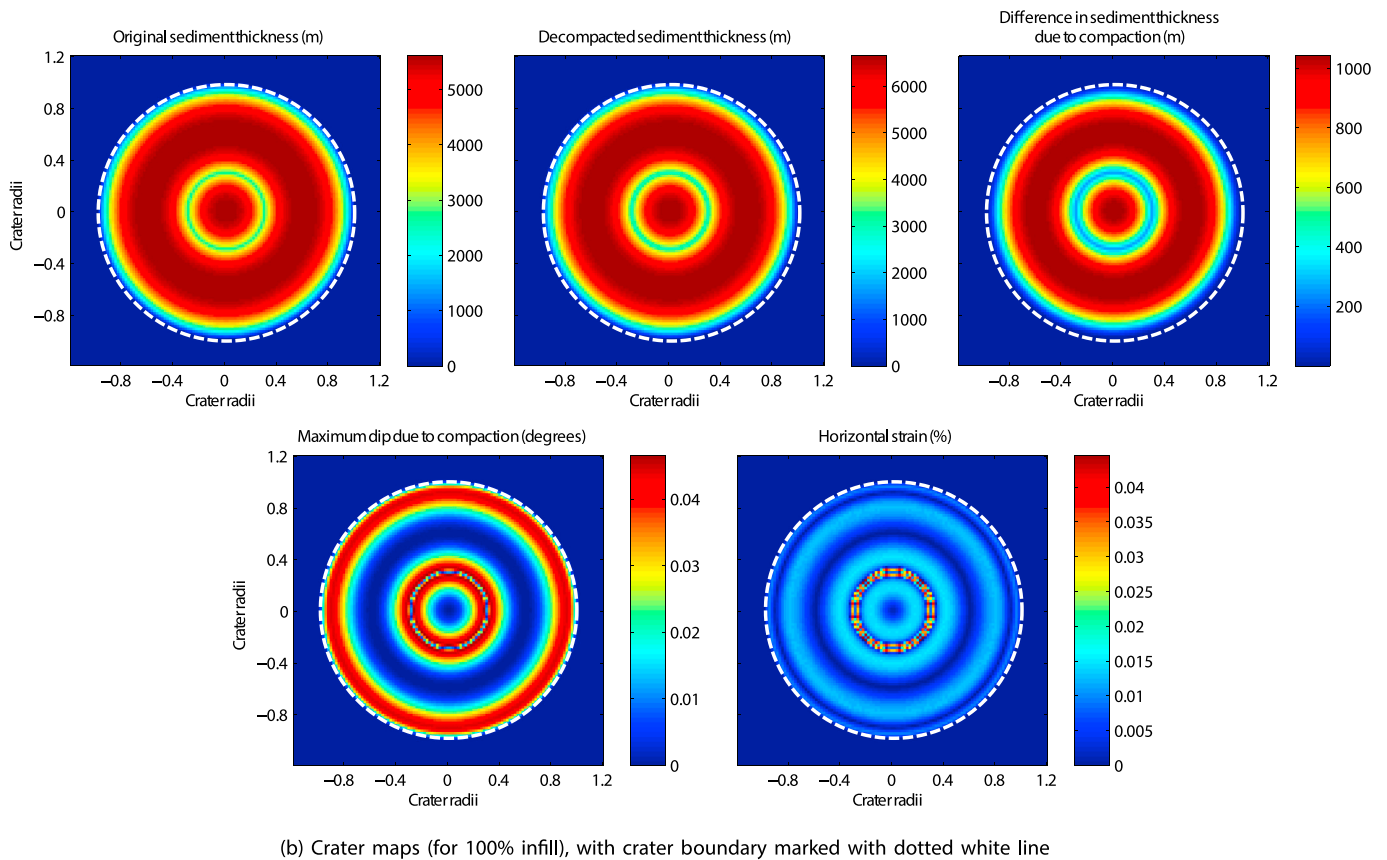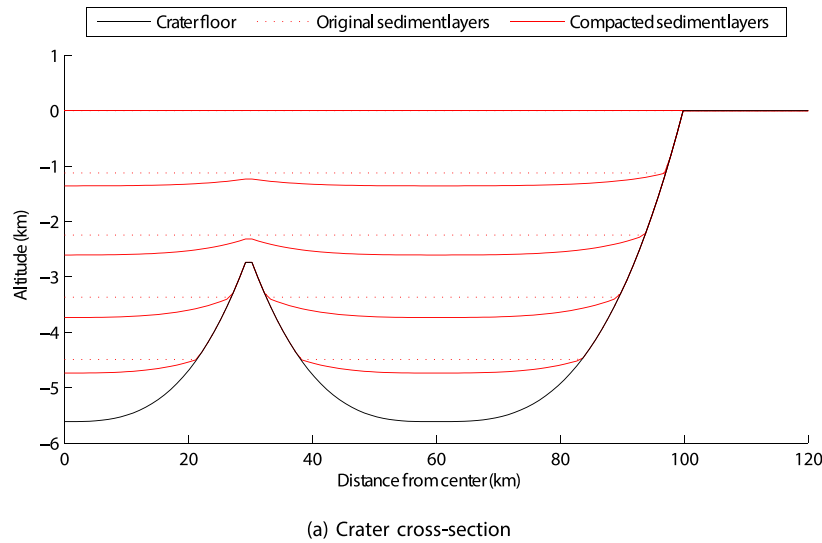
Fig. 3. Effect of sediment compaction modeled for an idealized central peak crater. Note that each map has its own individual colorbar, showing depth in m for sediment thickness, degrees for dip, and % for horizontal strain.

ment from a pristine crater profile. We select Tooting crater as a well-studied (Mouginis-Mark and Boyce, 2012) pristine crater of similar size to Gunjur, appropriately scaled and positioned (for each of our 120 radial topographic profiles) to have zero sediment depth at the crater peak and rim. (This "reference crater" approach has been used previously: see Grant et al. (2008b, 2016)). We use the complex-crater scaling equation from Tornabene et al. (2013), where diameter D and depth d are related by $d = 0.357D^{0.56}$ – this is the rule for deeper craters, which will allow a thicker sediment layer and so let us evaluate the maximal possible effect of compaction. We now have a sediment column for each measurement, and can calculate their compaction.

We interpolate a 100×100 grid from the profiles in order to calculate the maximal x-y gradient. This gives us a map of the dip induced by compaction. We run this calculation multiple times for different infill types and different infill thicknesses. This gives us a range of compaction dip maps possible for Gunjur. Fig. 8 shows a discrete categorization of the results, i.e. maps showing high/low dip as well as high/low horizontal strain, for two extreme cases: sandstone infill with no overburden, for the smallest compaction case, and shale infill with 1000 m of overburden, for the largest compaction case we computed. Fig. A.21 shows the complete continuous version of these maps.

The grid interpolation process causes radial artifacts ("spokes") as a

(a) Crater cross-section

(b) Crater maps (for 100% infill), with crater boundary marked with dotted white line

Fig. 4. Effect of sediment compaction modeled for an idealized peak ring crater. Note that each map has its own individual colorbar, showing depth in m for sediment thickness, degrees for dip, and % for horizontal strain.

side effect, which we reduce by circular smoothing with a 1-D mean filter of width 3.

Fig. 8 and Appendix A show that areas of significant dip are arranged concentrically, as expected. There is a wide band close to the crater rim (but separated from it by a ~1 km annulus of low dips). There are also arcs around several of the alluvial fans/deltas, notably in the south.

In studying the locations of the graben, we can see that they lie within or near the areas of high horizontal strain. Not all these areas are associated with graben, but most of the graben that are present are found in such areas. Of particular importance is the graben to the E of the central peak: a significant strain area also appears there, but only for large

overburdens. It is not visible for the case of zero overburden, but quite prominent for the 1000 m case, favoring the latter infilling scenario. Additionally, in referring to the values given in Jachens and Holzer (1982), we note that while faulting has been observed for strain values as low as 0.02%, it is much more likely for values above 1%, which again favors the 1000 m shale infill scenario.

Therefore, one possible explanation of the pattern of concentric dips is that Gunjur was almost completely filled by ≥ 1000 m of overburden that has since been removed (Malin and Edgett, 2000; Edgett and Malin, 2002). In this explanation, the build-up and removal of ≥1000 m of overburden must have occurred between two alluvial fan-forming
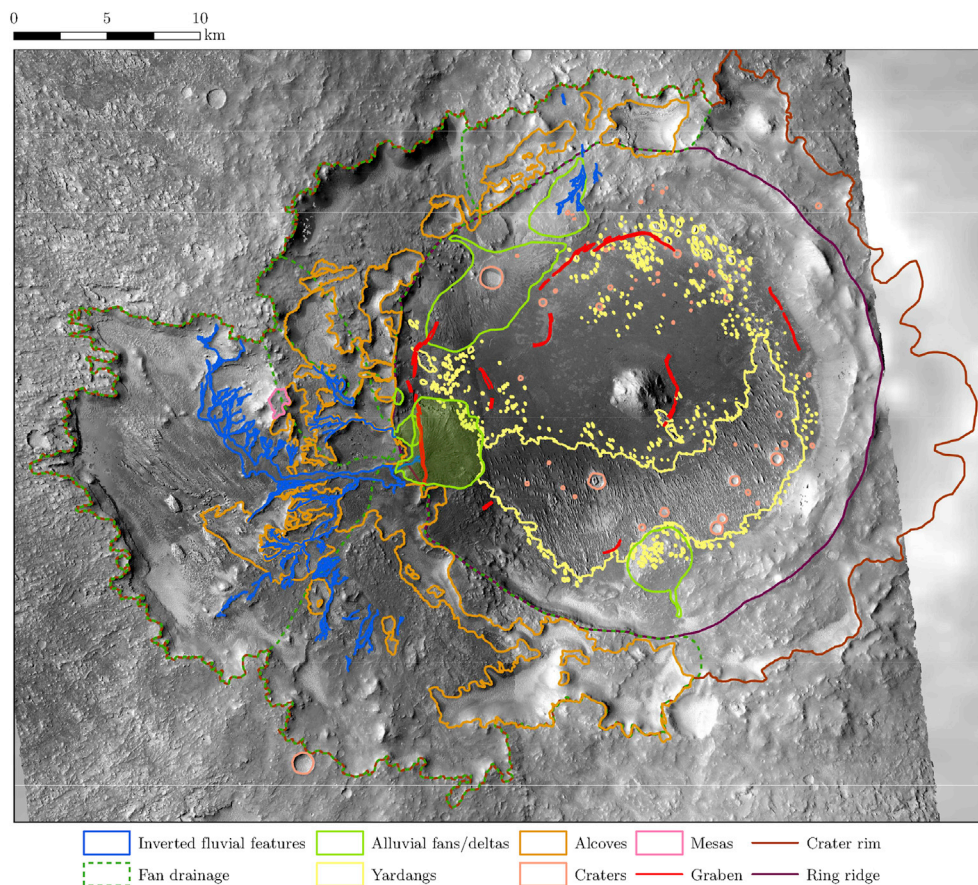
Fig. 5. Geomorphological map of Gunjur crater (0.2°S, 146.7°E, 27 km diameter), using CTX mosaics D15_033253_1798 and D15_033108_1798.

Inverted fluvial features	Alluvial fans/deltas	Alcoves	Mesas	Crater rim	
Fan drainage	Yardangs	Craters	Graben	Ring ridge	
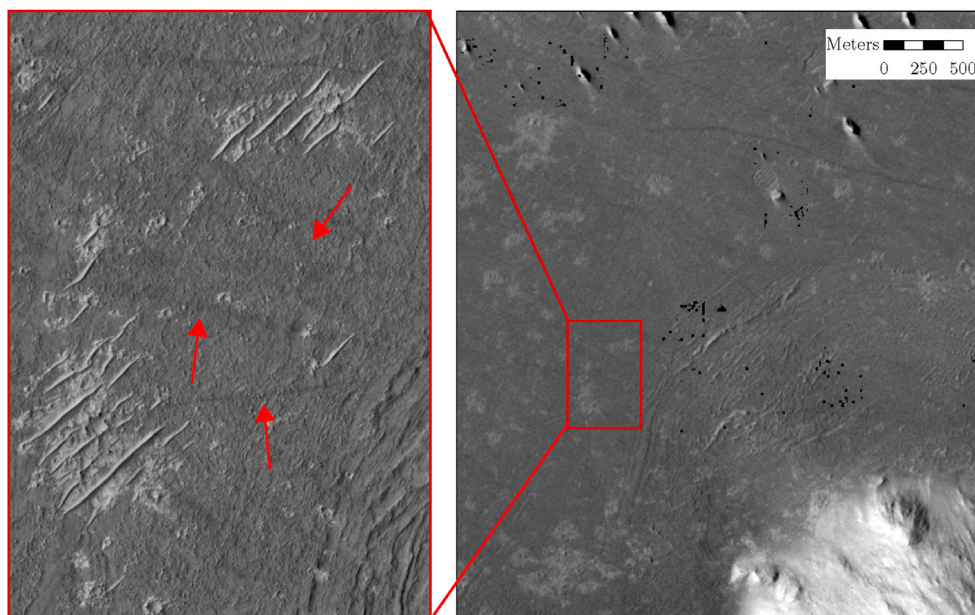
Fig. 6. Closeup image of paleochannels (marked with arrows), oriented NW-SE, visible in basin deposits to the NW of Gunjur's central peak. The paleochannels are sinuous lines, sometimes branching or overlapping, darker than the base deposits. (HiRISE image ESP_033108_1800_RED courtesy of NASA/JPL/University of Arizona). (For interpretation of the references to color in this figure legend, the reader is referred to the Web version of this article.)

episodes. One alternative explanation is that subsurface sediments near Gunjur's central peak were sourced from Gunjur's central peak. In that case, there would be a grain size (compactibility) gradient away from Gunjur's central peak, and this could lead to a greater compaction gradient corresponding to the gravel-sand transition (Lamb and Venditti, 2016). However, we have not observed any paleochannels leading away from the peak to support this hypothesis. Another alternative explanation is that the Gunjur stratigraphy contained massive ice, which was lost to the atmosphere by sublimation, causing subsidence. This, however, would likely have produced characteristic geomorphological features
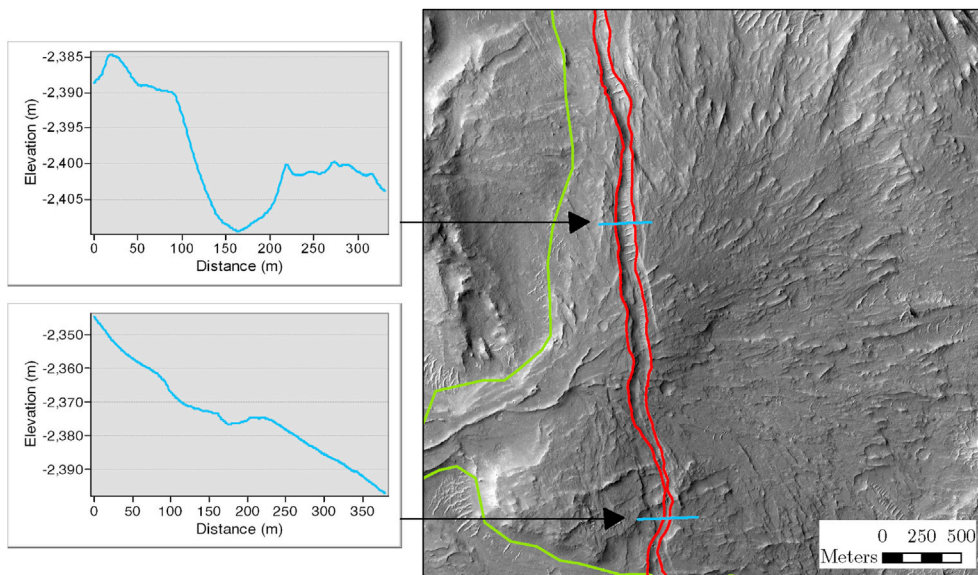
Fig. 7. Closeup of a graben (in red) crossing an alluvial fan (outlined in green), located on the W edge of the crater. Two topographic profiles of the graben in different locations (in blue) show graben's width and depth. (HiRISE image PSP_007883_1800 courtesy of NASA/JPL/University of Arizona). (For interpretation of the references to color in this figure legend, the reader is referred to the Web version of this article.)

such as pitting (Mangold, 2011), which we do not observe in the area. The past-overburden hypothesis seems to be the simplest of these three explanations.

The timescales necessary for the build-up and erosion of 1000 m of overburden are consistent with martian geologic history: intense fluvial activity on Mars spanned a minimum of 100–300 Ma (Kite et al., 2017), and deposition of at least 1.2 km of sediment, followed by relatively rapid erosion and superposition of alluvial fans, has been observed in Gale Crater (Caswell and Milliken, 2017).

The possibility of rapid build-up of overburden followed by complete or near-complete removal of is geologically reasonable. $> 1 \ \mu m \cdot yr^{-1}$ of sediment build-up and removal are also inferred at W Arabia Terra (Zabrusky et al., 2012), for the Medusae Fossae Formation (Kerber and Head, 2012), and for Mars layered sediments more broadly (Lewis and Aharonson, 2014).

One reason why rapid build-up and removal is important is because it complicates delta interpretations. Delta identification is straightforward if clinoforms can be measured; however, this has been done for few Martian locations so far (Jezero crater (Goudge et al., 2017), Eberswalde crater (Lewis and Aharonson, 2006), Terby crater (Ansan et al., 2011) and Melas Chasma (Dromart et al., 2007)), due to generally poor clinoform preservation. In absence of these measurements, deltas have been identified via locating fan-shaped landforms with a steep drop-off at their edge (Palucis et al., 2016), which may superficially resemble the boundary of a lake. However, this assumption neglects the possibility that the fan was extended past its present boundary with fine-grained deposits which have since been eroded.

Terrestrial analogs for compaction-driven circumferential faulting at Gunjur include polygonal faulting in fine-grained sediments (Lonergan et al., 1998), and subsidence in areas of groundwater or oil withdrawal. In the case of subsidence due to groundwater or oil withdrawal, faulting is commonly high-angle, normal, and peripheral to the subsidence bowl. Examples include Goose Creek and Mykawa, both in Texas; and Inglewood (Castle and Yerkes, 1976) and Kern Front (Castle, 1983), both in California. These attributes are consistent with the graben at Gunjur.

At Gunjur, circumferential faults plausibly caused by differential compaction are a stratigraphic marker separating two phases of alluvial-fan activity. Because time is required for the fluid escape which must accompany compaction, the compaction explanation sets a lower bound on the interval separating the two phases of alluvial-fan activity: Kooi and de Vries (1998) estimate that the compaction timescale of shale can reach 10^5–10^7 years for thick low-permeability layers. Time is also required for the build-up and then removal of sediment in the

thick-overburden hypothesis.

4. Compaction and layer dips at Gale

Gale is a 155-km diameter crater that contains a 5 km-high sediment mound – Mount Sharp – that is the main target for the Curiosity rover. The moat surrounding the mound contains at least one delta (Irwin et al., 2005; Palucis et al., 2016), and Curiosity has found alluvial-fan and probable lacustrine sediments in the moat (Williams et al., 2013; Grotzinger et al., 2014). Large-scale layer orientations are near-horizontal for the probable lacustrine sediments explored by Curiosity in Gale's moat (Grotzinger et al., 2015). However, layer orientations mapped by many workers within Gale's mound (Stack et al., 2013; Deit et al., 2013; Kite et al., 2013, 2016) dip systematically away from the center of the Gale mound. The data from Kite et al. (2016) are summarized in Table 2, and have been exhaustively tested (Kite et al., 2016, Section 2) to ensure that they form an accurate and consistent dataset.

Because the moat sediments have some thickness (Hurowitz et al., 2017; Buz et al., 2017) and because the mound must have once been more extensive (because layers are exposed in the flanks of the mound), compaction must have occurred within Gale. Grotzinger et al. (2015) argue that compaction may account for the Gale mound layer orientations. To explain this, Grotzinger et al. (2015) assume a rigid indentor basal topography that dips smoothly (constant slope) away from Gale's central peak. If the level where the dips are measured is 4.5 km below and 40 km away from Gale's central peak, then a shale pile 10 km thick will be compacted by 53%, leading to dips of 4°.

A concern with this scenario is that central peaks do not resemble the smoothly-dipping rigid indentor assumed by Grotzinger et al. (2015). Rather, radial profiles of complex craters show a "bowl" shape (see Fig. 6.9 of Melosh, 2011). Because the measured layer orientations at Gale correspond to the bottom of the "bowl", dips are gentle. We can empirically quantify this by drawing radial profiles for "pristine" complex craters on Mars. To adjust these profiles to Gale's size, we use the complex-crater scaling of Tornabene as described in §3.

We examine several possibilities for the shape of the pristine basal surface:

1. Gale is a central-peak crater, with Mount Sharp being built atop an existing smaller peak. Two further cases exist:
   (a) The sediment infill in Gale does not completely cover the basin, and the lowest part of the extant basin surface represents the

(a) Sandstone infill with no overburden

(b) Shale infill with 1000 m of overburden.
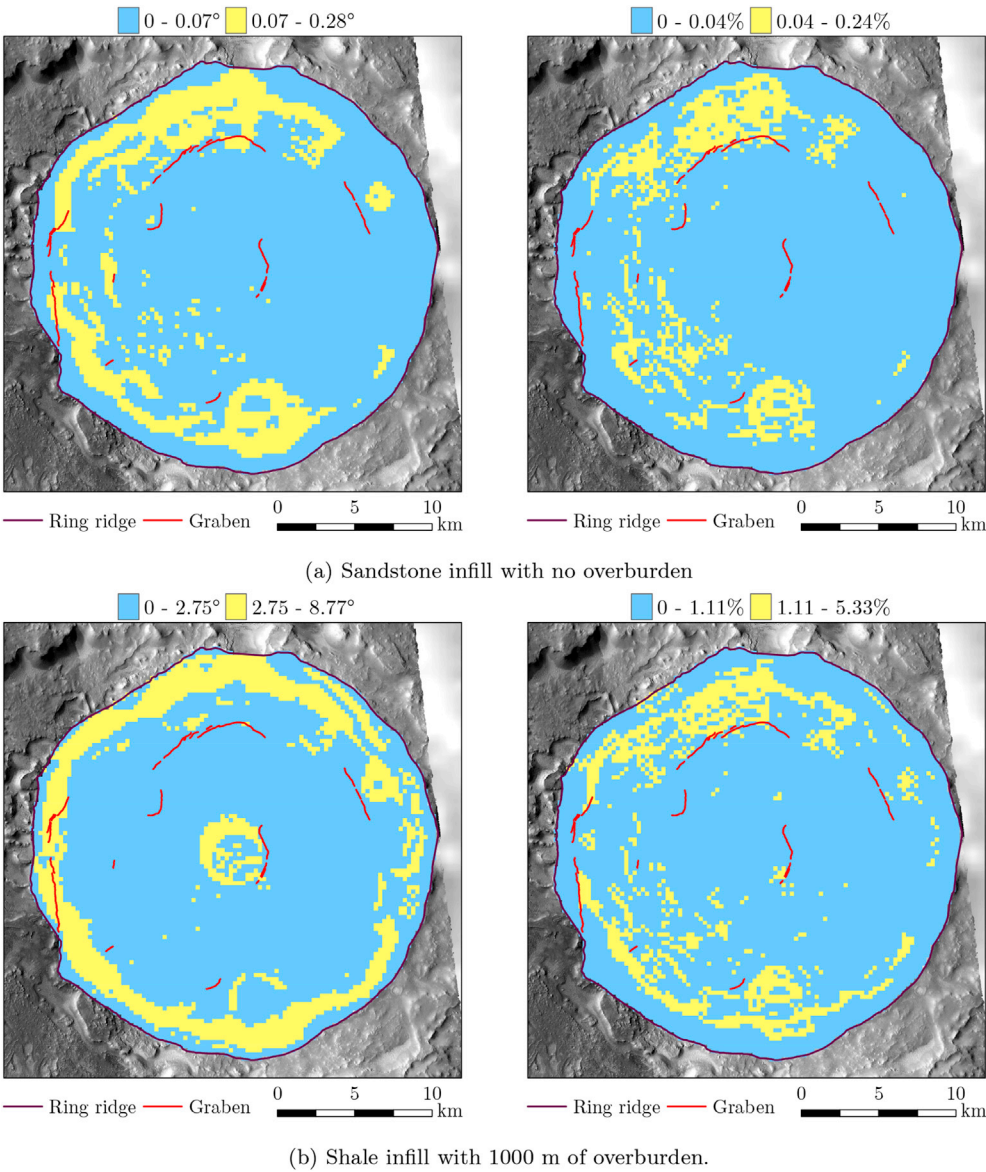
Fig. 8. Maps of the maximal dip due to compaction (left column) and the horizontal strain (right column) for Gunjur crater with two different types of infill. NB: each map has its own discrete classification which uses Jenks natural breaks optimization to find the areas of high dip (in degrees) or high horizontal strain (in %). These are marked in yellow. (For interpretation of the references to color in this figure legend, the reader is referred to the Web version of this article.)

Table 2
Dip measurements (radially projected, away from crater center), azimuths (counter-clockwise from east) and locations (distance from center and elevation) in Gale crater. The elevations are detrended, i.e. the overall regional slope is compensated for.

Azimuth from center (°)	6.11	149.42	158.15	−21.78	32.6	174.06	18.44	154.47	137.17	124.95	115.73
Distance from center (km)	15.98	24.84	32.27	33.94	38.8	39.47	39.63	41.7	42.64	43.72	45.99
Elevation (km)	−1.15	−1.12	−1.35	−2.27	−1.15	−2.38	−1.37	−2.35	−2.17	−2.29	−2.54
Dip (°)	7.91	2.96	4.16	0.86	2.81	4.09	1.72	3.52	3.01	4.09	2.94

pristine floor. We use a N-S profile taken through the **south section of Gale** for this.

(b) The sediment infill has completely obscured the original crater floor. We must use an appropriately scaled pristine central-peak crater, in this case **Tooting**, as the pristine floor.

2. Gale is a peak-ring crater. The ring is concealed under Mount Sharp, which is composed entirely of sediment. We select a pristine peak-ring crater – **Galle** – to act as the pristine floor.

Fig. 9 shows all three possible basal topographies as well as the crater profile from Grotzinger et al. (2015), keeping in mind that it is quite schematic and the scale may be imprecise.

For each possible topography, we generate sediment columns in the measured layer dip locations, and calculate the column heights and surface slope resulting from compaction based on the initial column thicknesses dictated by the shape of the infill. We use the compaction parameters for shale as given by Hantschel and Kauerauf (2009) as the most compactible material which will result in the highest possible degree of dip.

For compaction to rotate layers away from the crater center, either the basal topography must dip quite steeply away from the crater center, or the top surface of the now-vanished overburden must dip quite steeply toward the crater center. In order to quantify the ability of the basal topography to dip quite steeply away from the crater center, we introduce the concept of *maximum basal slope*. The maximum basal slope for a pristine crater is the elevation at the foot of the central peak (15 km from
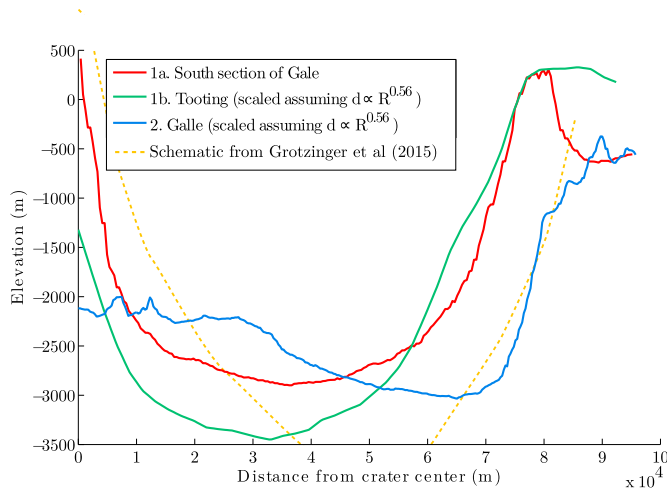
Fig. 9. Basal topography profiles, scaled to the diameter of Gale after Tornabene et al. (2013), and the schematic profile from Grotzinger et al. (2015).

the crater center), minus the bottom elevation of the crater, divided by the horizontal distance from the bottom elevation to 15 km. Because central peaks are steep-sided, the maximum basal slope for Gale is quite gentle – 0.94 ° based on the south section of Gale, 1.09 ° based on Tooting crater, and 0.91° based on Galle crater.

Because the basal topography is flat or gently sloping, filling up Gale with a layer-cake (cylinder) of initially-horizontal layers does not lead to great deflection from the horizontal.[2] We are unable to match the layer orientations that are observed with compaction with this single-parameter model (see Figs. 10–12).

This changes if we allow the now-vanished overburden to have a rugged top topography. An overburden that is thick near the edge of the crater and thins out near the crater peak will produce dips that are oriented outwards, as observed. This is qualitatively plausible: for example, if sediment is sourced from the crater rim, then the sediment fill should be thicker near the edge of the crater than near the center. To allow for more complex crater overburden shapes, we use Chebyshev polynomials (Mahanti et al., 2014). Chebyshev polynomials of the first kind are defined by the following recurrence equation:

$$T_0(x) = 1$$

$$T_1(x) = x$$

$$T_{n+1}(x) = 2x \times T_n(x) - T_{n-1}(x)$$

We suppose that the sedimentary fill is axi-symmetric. This means we are constrained to even-degree polynomials for defining the shape of the infill surface. We also restrain ourselves to degree 4 and lower, as more complex infill shapes are physically improbable. The shapes described by even-degree Chebyshev polynomials of degree 0, 2 and 4 are as follows, and are shown on Fig. 13.

Degree 0: simplest case, flat horizontal line. $T_0(x) = 1$
Degree 2: parabola. $T_2(x) = 2x^2 - 1$
Degree 4: symmetric quartic curve. $T_4(x) = 8x^4 - 8x^2 + 1$

We sum these polynomials, weighted by coefficients k_0, k_2 and k_4, to create a series, which describes the surface of the infill (Eq. (6)).

$$z_{sed} = k_0 + k_2 \times \left(2x^2 - 1\right) + k_4 \times \left(8x^4 - 8x^2 + 1\right) \qquad (6)$$

---

[2] We compute the rotation of initially-horizontal layers, but this can easily be applied to the rotation of initially-dipping layers (e.g., clinoforms).

To select an appropriate infill shape, we systematically scan a certain range for each Chebyshev coefficient in use. Specifically, for sediment thickness given in meters, the ranges are the following:

$$k_0 \in \left[-3 \times 10^4; 3 \times 10^4 \right]$$

$$k_2 \in \left[-6 \times 10^{-6}; 6 \times 10^{-6} \right]$$

$$k_4 \in \left[-5 \times 10^{-16}; 5 \times 10^{-16} \right]$$

The limit values were chosen arbitrarily to cover all physically probable outputs.

For each set of coefficients, we (i) create a curve defining the infill surface, (ii) calculate the sediment thickness and compaction, and (iii) compute the layer dip generated and the error relative to observed dips. We store the scan results in the form of two matrices containing the infill thickness and the root mean squared error on the dip measurements, and can subsequently optimize the infill shape by either of these parameters. The **root mean squared error** (RMSE) is the main parameter allowing us to quantify the fit of the model to the measurements, and is calculated by taking the root of the mean squared error, i.e. the average of the squares of the deviations between the modeled and measured dips.

Figs. 14–16 show the infill shape modeled with a 2-degree Chebyshev polynomial, optimized for minimal sediment thickness while remaining at a low root mean squared error (RMSE ≤ 3.3° for south Gale and Tooting, ≤ 3° for Galle). All three basal topographies result in physically improbable sediment thicknesses. It is impossible to obtain RMSE ≤ 3.2° with south Gale and Tooting as a basal topography; RMSE = 2.47° is possible for Galle basal topography, but with a significantly thicker sediment load than that shown in Fig. 16.

Figs. 17–19 show the infill shape according to the 4-degree Chebyshev model, optimized by sediment thickness with RMSE ≤ 3.3° for scaled-Tooting basal topography and scaled-South-Gale basal topography, and RMSE ≤ 2.5° for Galle basal topography (the RMSE values being close to the minimal obtainable values for any infill thickness). The infill using Tooting and south Gale as a basal topography remains at an improbable thickness around the rim. A new result is obtained for Galle basal topography: a torus shape is generated, with the sediment load thick in the center of the profile but thinning out towards the rim. The maximal torus thickness is approximately 8 km, but a significantly flatter and more realistic torus can be obtained by setting RMSE ≤ 3° (see Fig. 20).

It is interesting that steep dips away toward the canyon wall (away from the canyon center) are also found in HiRISE analyses of interior layered deposits in Mars canyons (e.g. Hore, 2015; Okubo et al., 2008; Kite et al., 2016). Mars canyons are not thought to have central peaks, so this suggests that dips toward the canyon (or crater) wall do not require a central peak.

We have also not observed compaction-induced faults (similar to those at Gunjur) at Gale, and are thus unable to use the same validation method as for Gunjur.

None of these issues are decisive; because compaction is sensitive to the local topography of the basal surface, and we cannot know the basal topography with certainty without active seismic surveys on Mars, we cannot rule out the compaction claim from orbit. While it is physically possible for sediment compaction to yield steep dips, this requires a basal surface that slopes strongly in the direction of the dip (peak-ring crater), highly compactible sediment (e.g. shale), and a torus-shaped sediment load. Therefore both the slope winds hypothesis (Kite et al., 2013, 2016) and the compaction hypothesis (Grotzinger et al., 2015) remain physically possible.

Fortunately, the origin of Mount Sharp's layer dips can be decisively tested by continued MSL exploration of the Gale mound: if compaction is responsible for dipping Mount Sharp's layers away from horizontal, then fluvial paleoflow directions (measured by high-resolution rover imagery of fine-scale bedform orientations and clast imbrication) will be "uphill"
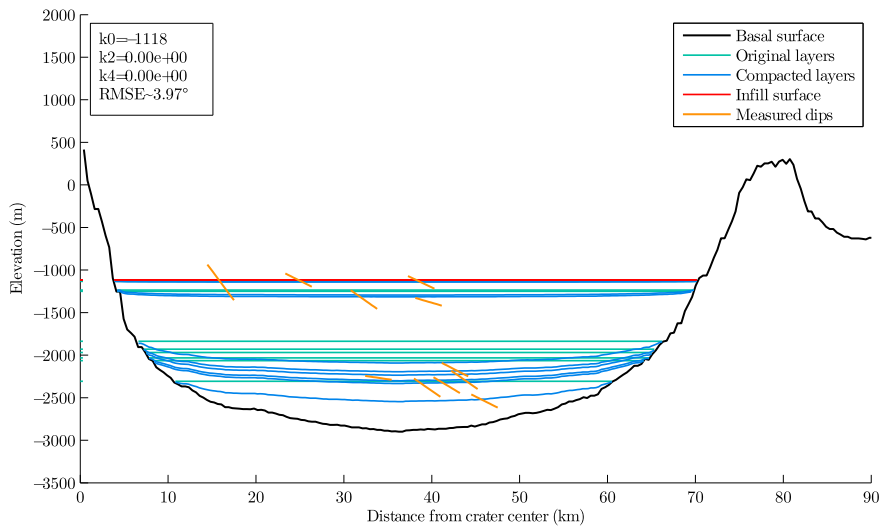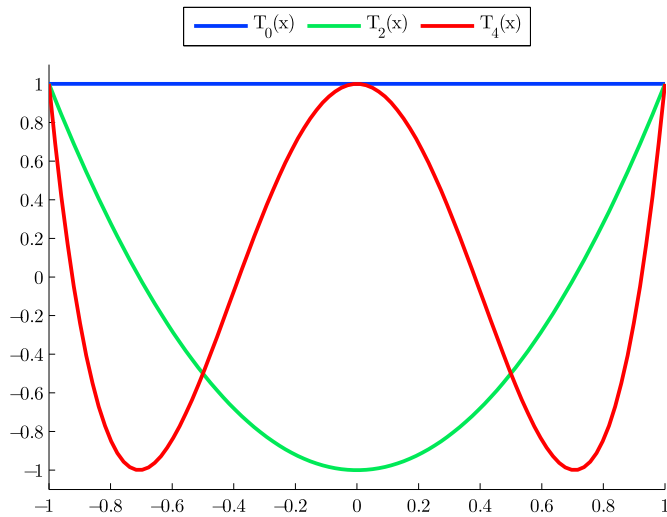
Fig. 10. Layer dips in Gale using the south section of Gale as basal topography with flat infill.
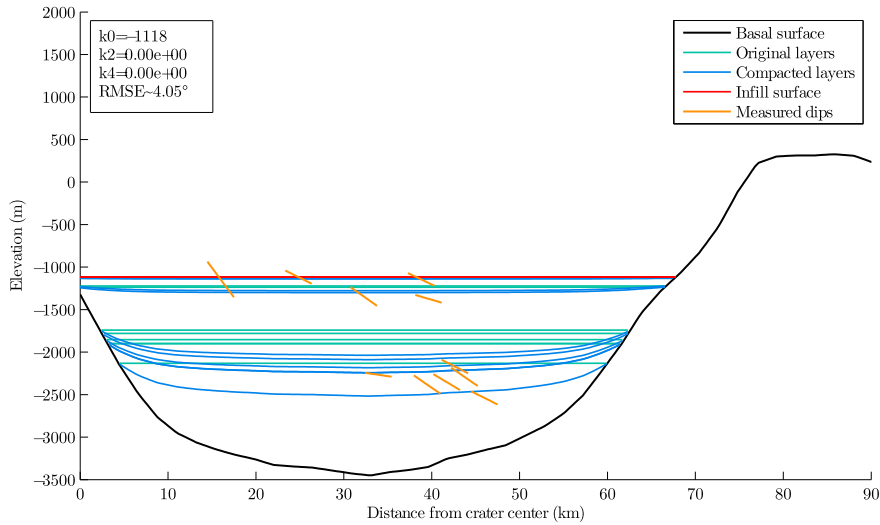
Fig. 11. Layer dips in Gale using Tooting as basal topography with flat infill.
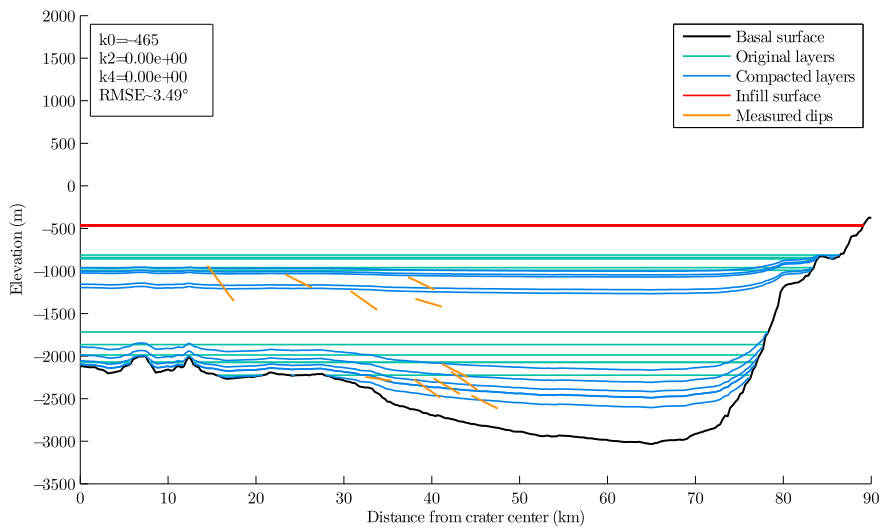
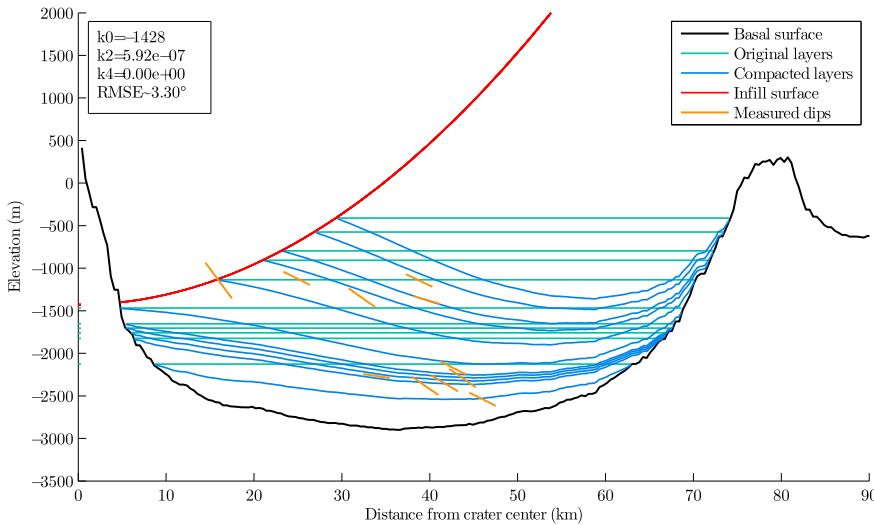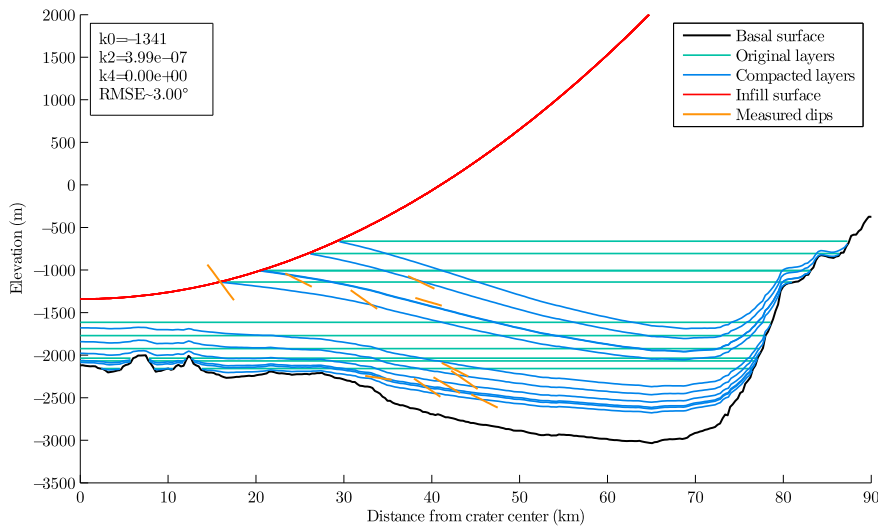**Fig. 12.** Layer dips in Gale using Galle as basal topography with flat infill.

Fig. 13. Plot of the first three even-degree Chebyshev polynomials: T_0, T_2 and T_4.

on modern topography. Compaction-driven dewatering may also provide a formation mechanism for the calcium sulfate veins at Gale observed by Curiosity (Nachon et al., 2014; Rapin et al., 2016).

5. Discussion

The sedimentary history of Gunjur has several discrete stages, as is evident from the distinct sediment volumes observed. The bulk of the infill was likely produced by fluvial transport, moving a large volume of sediment from the western flank of the crater into the basin proper. This formed the large alcove we observe today. The subsequent stage was the formation of alluvial fans, which itself occurred in two phases as can be seen from the graben, which postdate the larger fans but precede the smaller fans. From models, the existence of graben near the central peak favors a layer of overburden, to produce sufficient compaction for faulting. However, yardang-forming materials partially overlie the graben at the western edge of the crater, which appears to indicate either multiple phases of faulting or multiple phases of deposition of yardang-forming materials. Subsequent to the arrival of alluvial fans, compaction produced the concentric graben close to the main crater ring.

At Gunjur, gradients in compaction are maximal near the outer edge of the sediment fill and near the central peak, consistent with the locations of observed circumferential graben. More work is desirable to

Fig. 14. Layer dips in Gale using the south section of Gale as basal topography, with $\{k_0, k_2\}$ defining the infill shape.
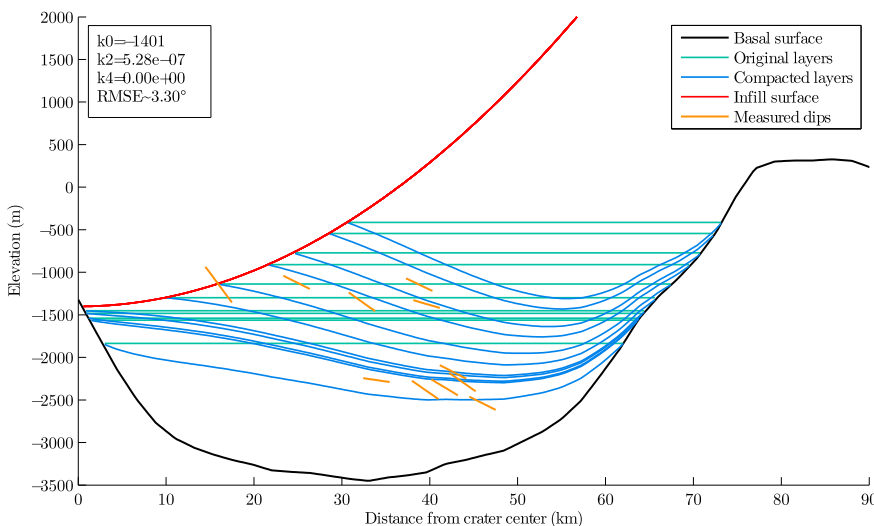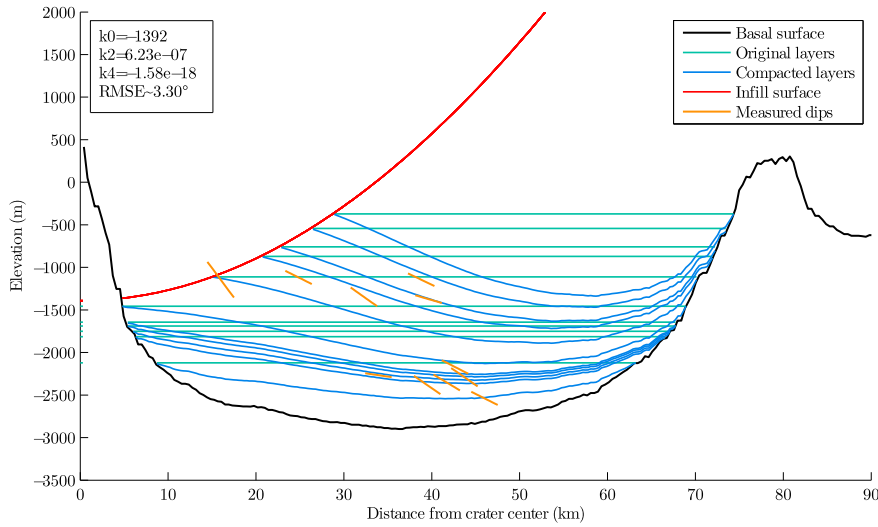

Fig. 15. Layer dips in Gale using Tooting as basal topography, with $\{k_0, k_2\}$ defining the infill shape.
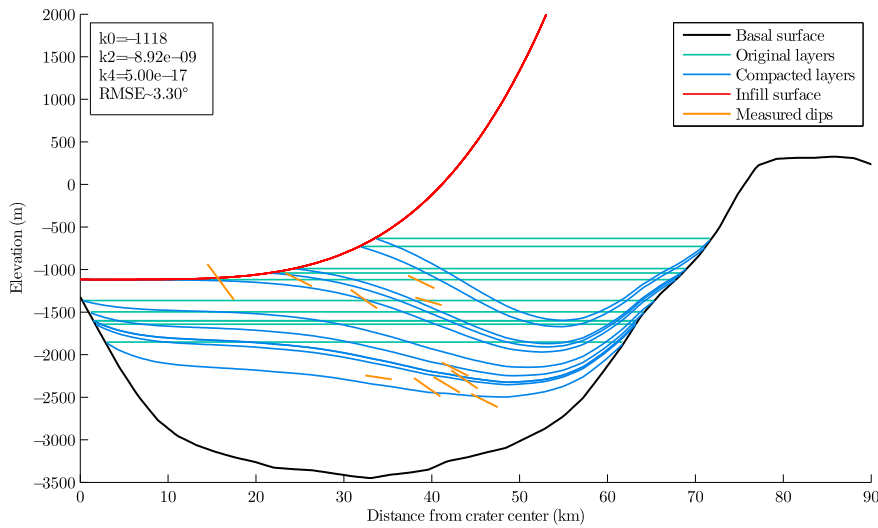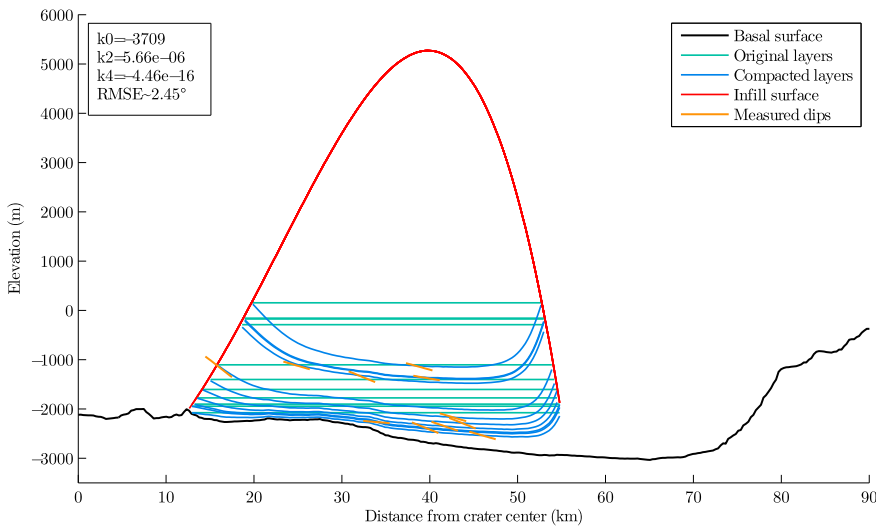
Fig. 16. Layer dips in Gale using Galle as basal topography, with $\{k_0, k_2\}$ defining the infill shape.
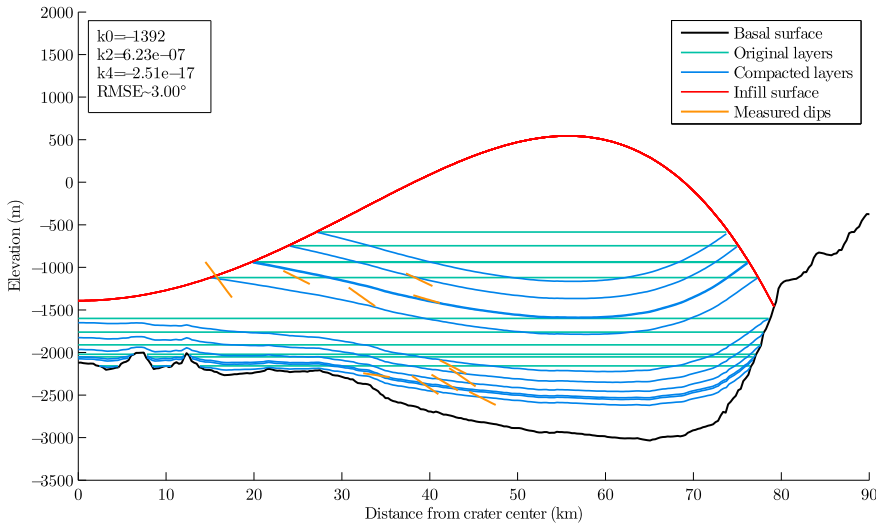

Fig. 17. Layer dips in Gale using the south section of Gale as basal topography, with $\{k_0, k_2, k_4\}$ defining the infill shape.

Fig. 18. Layer dips in Gale using Tooting as basal topography, with $\{k_0, k_2, k_4\}$ defining the infill shape.

Fig. 19. Layer dips in Gale using Galle as basal topography, with $\{k_0, k_2, k_4\}$ defining the infill shape and RMSE $\leq 2.5°$.

Fig. 20. Layer dips in Gale using Galle as basal topography, with $\{k_0, k_2, k_4\}$ RMSE $\leq 3°$ defining the infill shape and *RMSE* $\leq 3°$.

compare the strains predicted by the compaction model with graben offsets measured from HiRISE DTMs.

Assuming a differential compaction interpretation of the layer dip measurements at Gale, the combination of measurements and our models appear to support a basal topography that slopes gently away from the center of the basin. How might this condition occur? One possibility is that the pristine shape of Gale is that of a peak-ring crater, and sedimentary infill also occurred in multiple stages. First, we can posit fluvial transport which brought a large volume of sediment and likely filled most of the basin – this is the unit that forms Mount Sharp. After partial erosion of this sedimentary unit, aeolian transport may have occurred, depositing a further layer of sediment which would be thin or nonexistent close to the peak and thicker near the rim, feathering out again as it approached the crater edge. It is not immediately obvious what formative geological process in Gale could result in the torus shape generated using a 4th-degree polynomial and a peak-ring basal topography. However, "lumpy" sediment mounds such as this have been observed, notably by Desai and Murty (2013) in Nicholson crater. We propose an aeolian process as a formation method for this torus, as no non-aeolian processes known to be present at Gale would generate a torus of the required size and shape. Aeolian-produced tori have not been located elsewhere on Mars to date, but their formation may be possible in multidirectional wind regimes such as those responsible for other exotic martian dune shapes (Parteli

et al., 2009).

So far we have assumed that the sediment dewaters faster than it accumulates (no-overpressure situation). Alternatively, as in the Gulf of Mexico on Earth, the sediment may dewater at a rate that is comparable to or slower than the sediment accumulation rates (Appendix B). This "fast-sedimentation" limit requires low permeability, which is especially relevant to fine-grained sediments. However, the sedimentation rate of rocks on Mars has been calibrated by comparison of quasi-periodic layer thicknesses to Milankovitch frequencies, and this suggests generally slow ($<100\,\mu m/yr$) accumulation (Lewis and Aharonson, 2014) which means that slow-sedimentation is more appropriate.

6. Conclusions

- We calculate compaction for Martian sedimentary basins contained within impact craters, using the topography of empty impact craters of similar size as a proxy for basement elevation, and assuming a fast compaction rate relative to sedimentation.
- With these assumptions, we find that:
- The pattern of differential-compaction strains within Gunjur crater is consistent with the distribution of observed circumferential graben.

- The magnitude and direction of layer orientations within Gale crater can be matched by differential-compaction dipping, but only if past sediment overburden at Gale was torus-shaped and >3 km thick.

Appendix A. Supplementary data

Supplementary data related to this article can be found at https://doi.org/10.1016/j.pss.2017.12.021.

Appendix A. Full dip maps for Gunjur
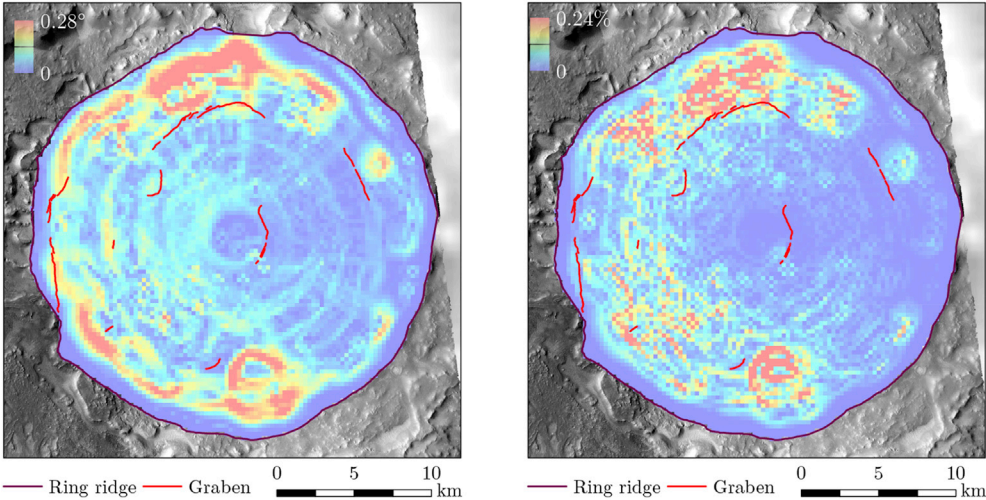
Figure A.21 Maps of the maximal dip due to compaction (left column) and the horizontal strain (right column) for Gunjur crater with two different types of infill. NB: each map has its own continuous colormap, showing dip in degrees and horizontal strain in %.

(a) Sandstone infill with no overburden
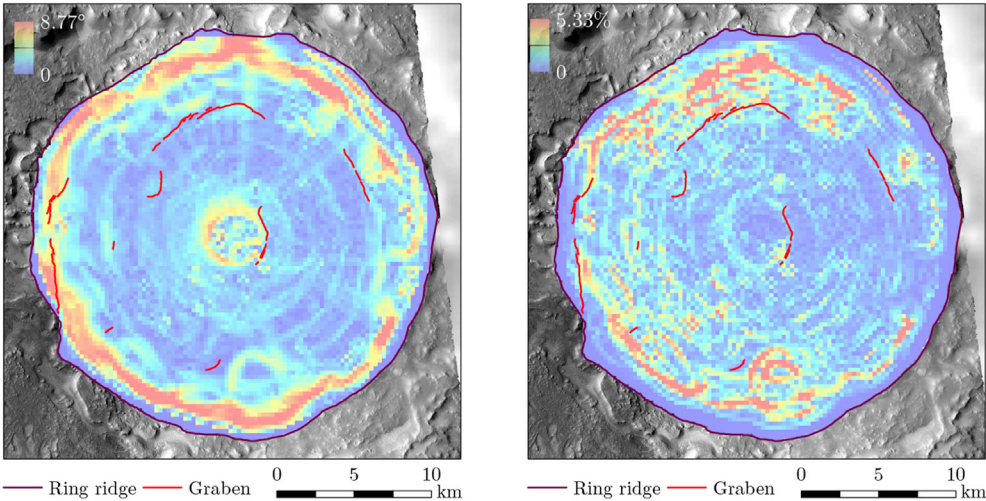
(b) Shale infill with 1000 m of overburden.

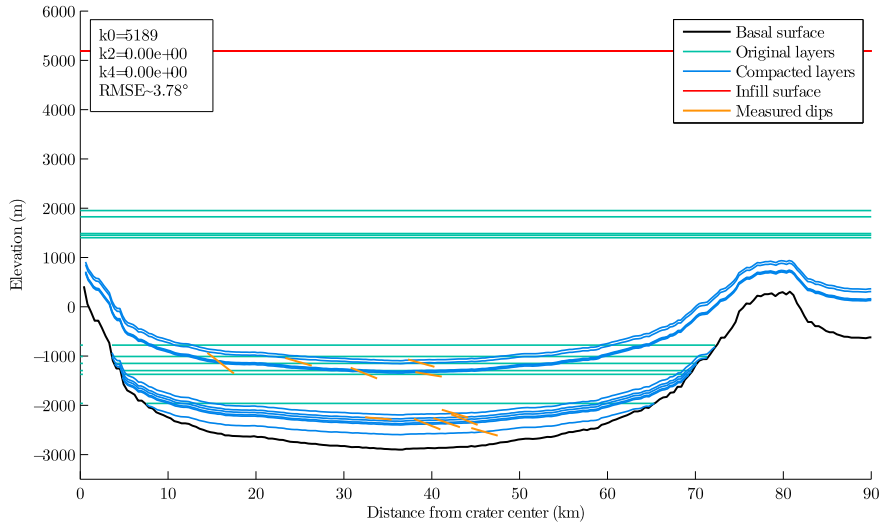## Appendix B. Slow compaction figures

Figure B.22 Layer dips in Gale using south Gale as basal topography, with flat infill and minimal RMSE.
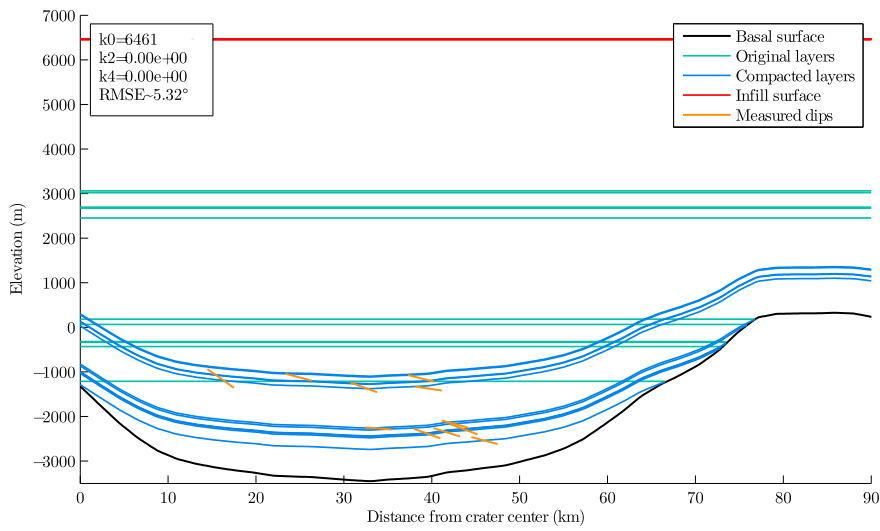

Figure B.23 Layer dips in Gale using Tooting as basal topography, with flat infill and minimal RMSE.
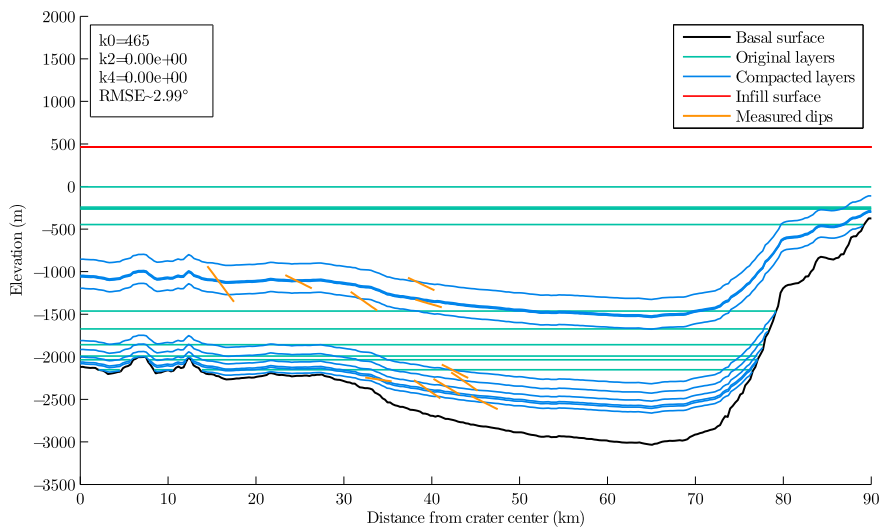

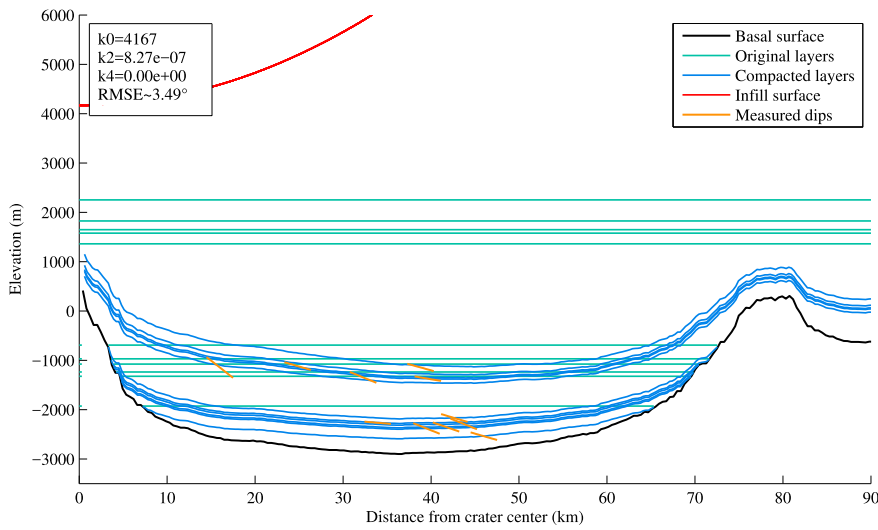Figure B.24 Layer dips in Gale using Galle as basal topography, with flat infill and RMSE $\leq 3°$.

Figure B.25 Layer dips in Gale using south Gale as basal topography, with $\{k_0, k_2\}$ defining the infill shape and RMSE $\leq$ 3.5°.

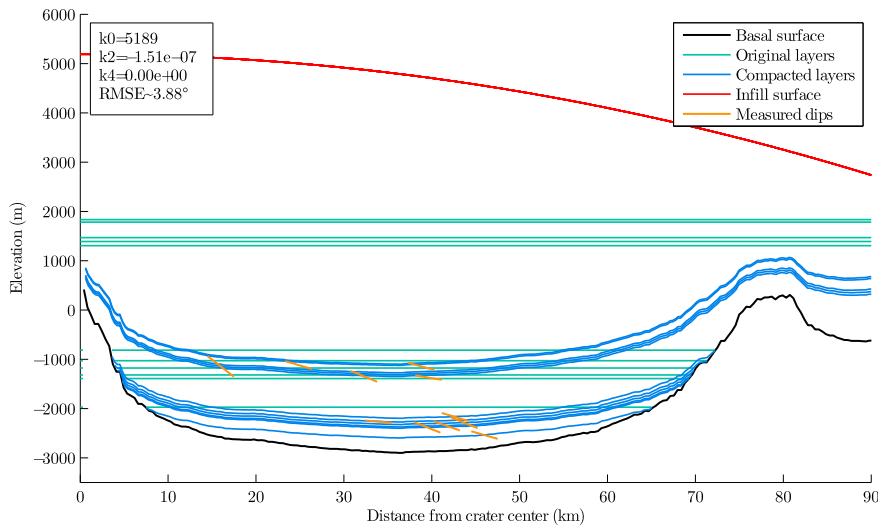Figure B.26 Layer dips in Gale using south Gale as basal topography, with $\{k_0, k_2\}$ defining the infill shape and RMSE $\leq$ 4°.
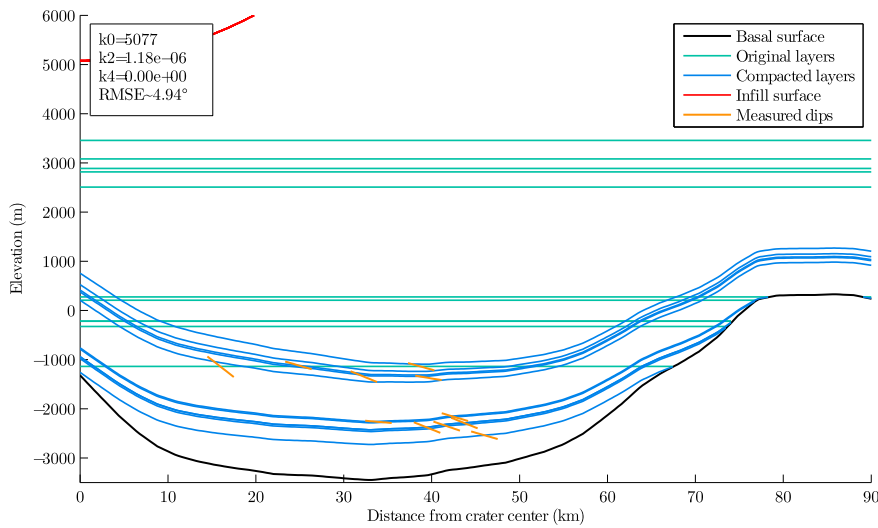

Figure B.27 Layer dips in Gale using Tooting as basal topography, with $\{k_0, k_2\}$ defining the infill shape and minimal RMSE.
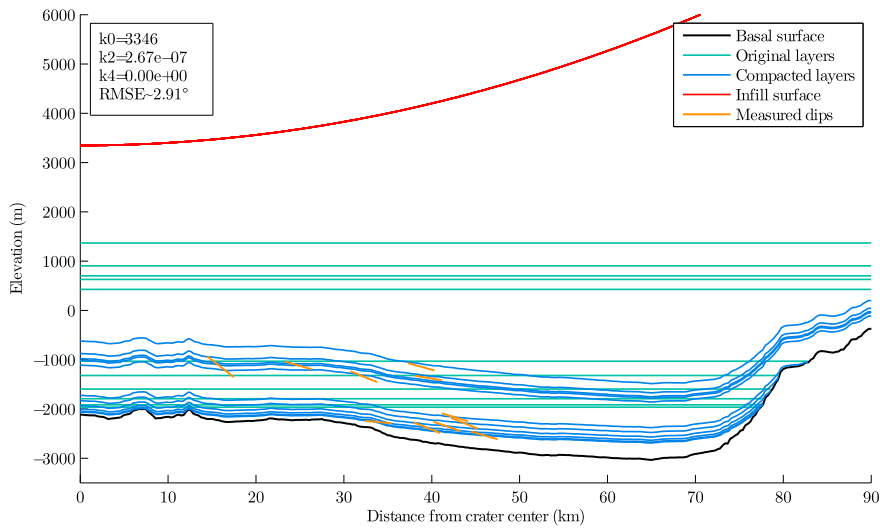
Figure B.28 Layer dips in Gale using Galle as basal topography, with $\{k_0, k_2\}$ defining the infill shape and minimal RMSE.

Figure B.29 Layer dips in Gale using Galle as basal topography, with $\{k_0, k_2\}$ defining the infill shape and RMSE $\leq 3°$.

Figure B.30 Layer dips in Gale using south Gale as basal topography, with $\{k_0, k_2, k_4\}$ defining the infill shape and minimal RMSE.

Figure B.31 Layer dips in Gale using south Gale as basal topography, with $\{k_0, k_2, k_4\}$ defining the infill shape and RMSE $\leq 4°$.

Figure B.32 Layer dips in Gale using Tooting as basal topography, with $\{k_0, k_2, k_4\}$ defining the infill shape and minimal RMSE.

Figure B.33 Layer dips in Gale using Galle as basal topography, with $\{k_0, k_2, k_4\}$ defining the infill shape and minimal RMSE.
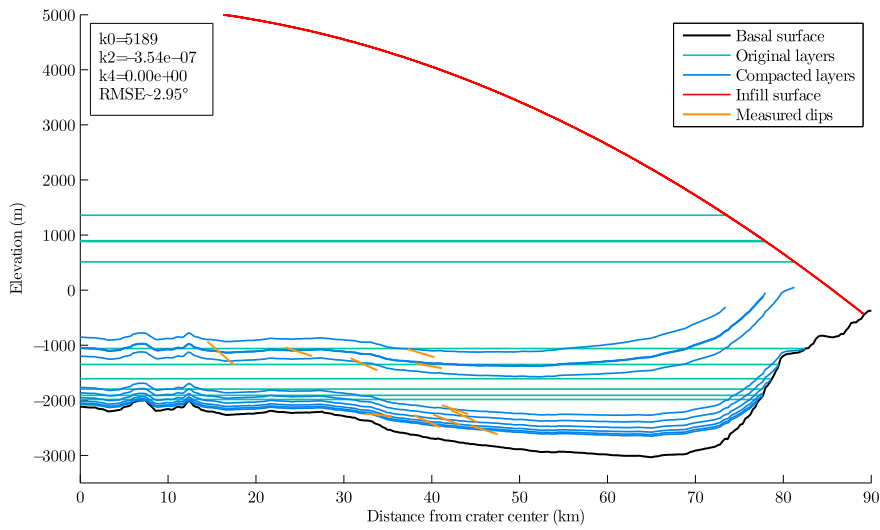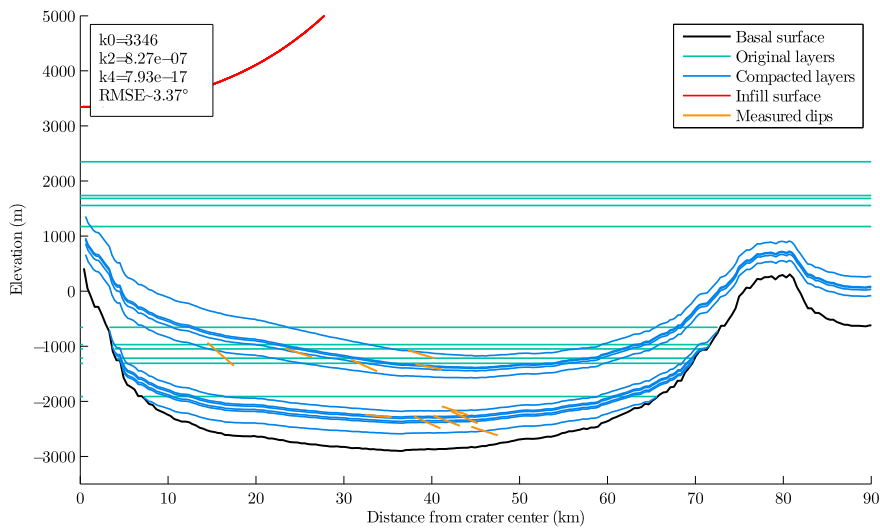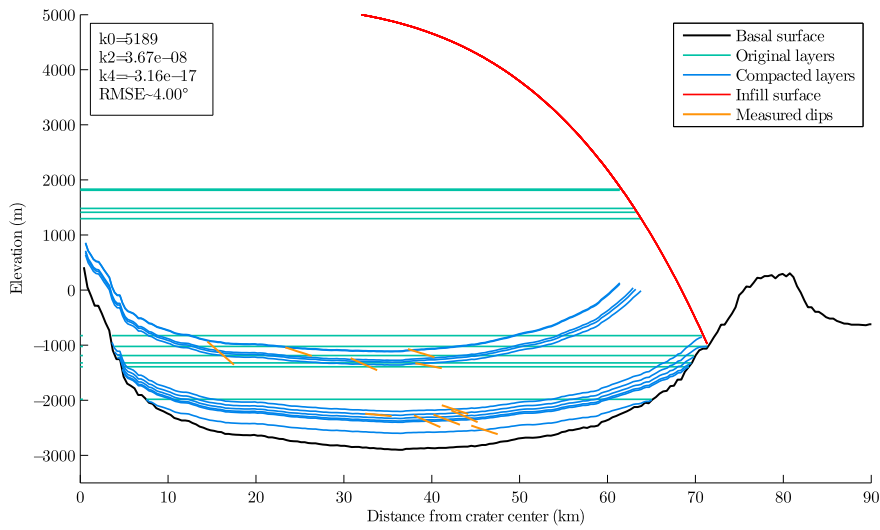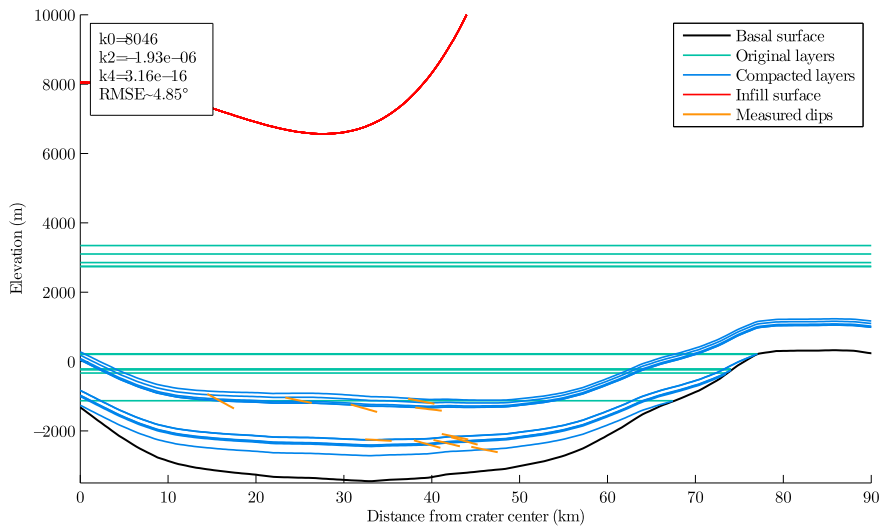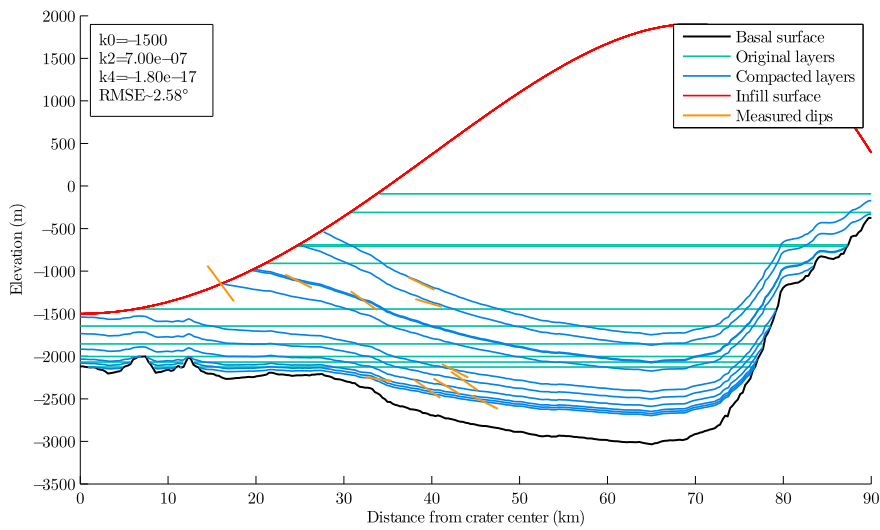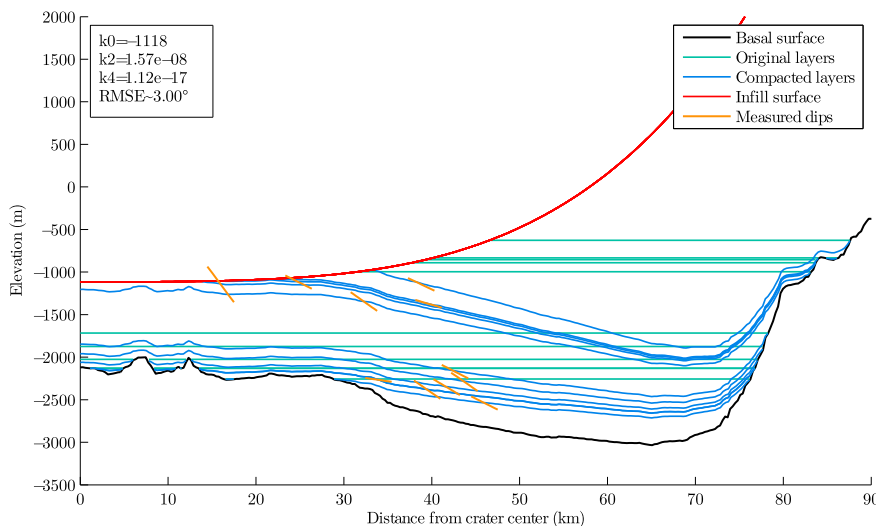
Figure B.34 Layer dips in Gale using Galle as basal topography, with $\{k_0, k_2, k_4\}$ defining the infill shape and RMSE $\leq 3°$.

References

Allen, Philip A., Allen, John R., 2005. Basin analysis: Principles and Applications. John Wiley & Sons.

Ansan, Véronique, Loizeau, D., Mangold, N., Le Mouélic, S., Carter, J., Poulet, F., Dromart, Gilles, Lucas, A., Bibring, J.-P., Gendrin, A., et al., 2011. Stratigraphy, mineralogy, and origin of layered deposits inside Terby crater, Mars. Icarus 211 (1), 273–304.

Athy, Lawrence Ferdinand, 1930. Density, porosity, and compaction of sedimentary rocks. AAPG Bull. 14 (1), 1–24.

Baldwin, Brewster, Butler, Crispin O., 1985. Compaction curves. AAPG Bull. 69 (4), 622–626.

Branney, Michael J., 1995. Downsag and extension at calderas: new perspectives on collapse geometries from ice-melt, mining, and volcanic subsidence. Bull. Volcanol. 57 (5), 303–318.

Buczkowski, Debra L., Cooke, Michele L., 2004. Formation of double-ring circular grabens due to volumetric compaction over buried impact craters: implications for thickness and nature of cover material in Utopia Planitia, Mars. J. Geogr. Reg. Planets 109 (E2).

Burr, D.M., Enga, M.-T., Williams, R.M.E., Zimbelman, J.R., Howard, A.D., Brennand, T.A., March 2009. Pervasive aqueous paleoflow features in the Aeolis/Zephyria Plana region, Mars. Icarus 200, 52–76. https://doi.org/10.1016/j.icarus.2008.10.014.

Buz, Jennifer, Ehlmann, Bethany L., Pan, Lu, Grotzinger, John P., 2017. Mineralogy and stratigraphy of the gale crater rim, wall, and floor units. J. Geogr. Reg. Planets 122 (5), 1090–1118. https://doi.org/10.1002/2016JE005163. ISSN 2169-9100.

Cailleau, Beatrice, Walter, Thomas R., Janle, Peter, Hauber, Ernst, 2003. Modeling volcanic deformation in a regional stress field: implications for the formation of graben structures on Alba Patera, Mars. J. Geogr. Reg. Planets 108 (E12).

Castle, R.O., Yerkes, R.F., 1976. Recent Surface Movements in the Baldwin Hills, Los Angeles, California, vol. 882. United States Department of the Interior. Geological Survey Professional Paper.

Castle, Robert, 1983. Historical Surface Deformation Near Oildale, California, vol. 1245. US Geological Survey Professional Paper.

Caswell, Tess E., Milliken, Ralph E., 2017. Evidence for hydraulic fracturing at Gale crater, Mars: implications for burial depth of the Yellowknife Bay formation. Earth Planet Sci. Lett. 468, 72–84.

Deit, Laetitia Le, Hauber, Ernst, Fueten, Frank, Pondrelli, Monica, Pio Rossi, Angelo, Jaumann, Ralf, 2013. Sequence of infilling events in Gale crater, Mars: results from morphology, stratigraphy, and mineralogy. J. Geogr. Reg. Planets 118 (12), 2439–2473.

Desai, Ami J., Murty, S.V.S., March 2013. Morphological investigations of Nicholson crater, Mars: identification of aeolian processes. In: Lunar and Planetary Science Conference, vol. 44, p. 1180.

Dromart, Gilles, Quantin, Cathy, Broucke, Olivier, 2007. Stratigraphic architectures spotted in southern Melas Chasma, Valles Marineris, Mars. Geology 35 (4), 363–366.

Edgett, Kenneth S., Malin, Michael C., 2002. Martian sedimentary rock stratigraphy: outcrops and interbedded craters of northwest Sinus Meridiani and southwest Arabia Terra. Geophys. Res. Lett. 29 (24).

Goudge, Timothy A., Milliken, Ralph E., Head, James W., Mustard, John F., Fassett, Caleb I., 2017. Sedimentological evidence for a deltaic origin of the western fan deposit in Jezero crater, Mars and implications for future exploration. Earth Planet Sci. Lett. 458, 357–365.

Grant, J.A., Parker, T.J., Crumpler, L.S., Wilson, S.A., Golombek, M.P., Mittlefehldt, D.W., 2016. The degradational history of Endeavour crater, Mars. Icarus 280, 22–36.

Grant, John A., Irwin, Rossman P., Grotzinger, John P., Milliken, Ralph E., Tornabene, Livio L., McEwen, Alfred S., Weitz, Catherine M., Squyres, Steven W., Glotch, Timothy D., Thomson, Brad J., 2008a. HiRISE imaging of impact megabreccia and sub-meter aqueous strata in Holden crater, Mars. Geology 36 (3), 195–198.

Grant, John A., Wilson, Sharon A., Cohen, Barbara A., Golombek, Matthew P., Geissler, Paul E., Sullivan, Robert J., Kirk, Randolph L., Parker, Timothy J., 2008b. Degradation of Victoria crater, Mars. J. Geogr. Reg. Planets 113 (E11).

Grotzinger, J.P., Sumner, D.Y., Kah, L.C., Stack, K., Gupta, S., Edgar, L., Rubin, D., Lewis, K., Schieber, J., Mangold, N., et al., 2014. A habitable fluvio-lacustrine environment at Yellowknife Bay, Gale crater, Mars. Science 343 (6169), 1242777.

Grotzinger, J.P., Gupta, S., Malin, M.C., Rubin, D.M., Schieber, J., Siebach, K., Sumner, D.Y., Stack, K.M., Vasavada, A.R., Arvidson, R.E., et al., 2015. Deposition, exhumation, and paleoclimate of an ancient lake deposit, Gale crater, Mars. Science 350 (6257), aac7575.

Hantschel, Thomas, Kauerauf, Armin I., 2009. Fundamentals of Basin and Petroleum Systems Modeling. Springer Science & Business Media.

Harrison, S.K., Balme, M.R., Hagermann, A., Murray, J.B., Muller, J.-P., Wilson, A., September 2013. A branching, positive relief network in the middle member of the Medusae Fossae Formation, equatorial Mars - evidence for sapping? Planet. Space Sci. 85, 142–163. https://doi.org/10.1016/j.pss.2013.06.004.

Hore, Alicia, 2015. Structural Analysis, Layer Thickness Measurements and Mineralogical Investigation of the Large Interior Layered Deposit within Ganges Chasma, Valles Marineris, Mars. PhD thesis. Brock University.

Hurowitz, J.A., Grotzinger, J.P., Fischer, W.W., McLennan, S.M., Milliken, R.E., Stein, N., Vasavada, A.R., Blake, D.F., Dehouck, E., Eigenbrode, J.L., Fairén, A.G., Frydenvang, J., Gellert, R., Grant, J.A., Gupta, S., Herkenhoff, K.E., Ming, D.W., Rampe, E.B., Schmidt, M.E., Siebach, K.L., Stack-Morgan, K., Sumner, D.Y., Wiens, R.C., June 2017. Redox stratification of an ancient lake in Gale crater, Mars. Science 356. https://doi.org/10.1126/science.aah6849.

Irwin, Rossman P., Howard, Alan D., Craddock, Robert A., Moore, Jeffrey M., 2005. An intense terminal epoch of widespread fluvial activity on early Mars: 2. Increased runoff and paleolake development. J. Geogr. Reg. Planets 110 (E12).

Jachens, Robert C., Holzer, Thomas L., 1982. Differential compaction mechanism for earth fissures near Casa Grande, Arizona. Geol. Soc. Am. Bull. 93 (10), 998–1012.

Kerber, L., Head, J.W., March 2012. A progression of induration in Medusae Fossae Formation transverse aeolian ridges: evidence for ancient aeolian bedforms and extensive reworking. Earth Surf. Process. Landforms 37, 422–433.

Kite, E.S., Sneed, J., Mayer, D.P., Lewis, K.W., Michaels, T.I., Hore, A., Rafkin, S.C.R., November 2016. Evolution of major sedimentary mounds on Mars: buildup via anticompensational stacking modulated by climate change. J. Geogr. Reg. Planets 121, 2282–2324. https://doi.org/10.1002/2016JE005135.

Kite, Edwin S., Lewis, Kevin W., Lamb, Michael P., Newman, Claire E., Richardson, Mark I., 2013. Growth and form of the mound in Gale crater, Mars: slope wind enhanced erosion and transport. Geology 41 (5), 543–546.

Kite, Edwin S., Howard, Alan D., Lucas, Antoine, Lewis, Kevin W., 2015a. Resolving the era of river-forming climates on Mars using stratigraphic logs of river-deposit dimensions. Earth Planet Sci. Lett. 420, 55–65.

Kite, Edwin S., Howard, Alan D., Lucas, Antoine S., Armstrong, John C., Aharonson, Oded, Lamb, Michael P., 2015b. Stratigraphy of Aeolis Dorsa, Mars: stratigraphic context of the great river deposits. Icarus 253, 223–242.

Kite, Edwin S., Sneed, Jonathan, Mayer, David P., Wilson, Sharon A., 2017. Persistent or repeated surface habitability on Mars during the late Hesperian-Amazonian. Geophys. Res. Lett. 44 (9), 3991–3999.

Kooi, H., de Vries, J.J., 1998. Land subsidence and hydrodynamic compaction of sedimentary basins. Hydrol. Earth Syst. Sci. 2, 159–171.

Lamb, M.P., Venditti, J.G., April 2016. The grain size gap and abrupt gravel-sand transitions in rivers due to suspension fallout. Geophys. Res. Lett. 43, 3777–3785. https://doi.org/10.1002/2016GL068713.

Lee, Kenneth L., Shen, C.K., 1969. Horizontal movements related to subsidence. J. Soil Mech. Found Div. 95, 139–166.

Lefort, Alexandra, Burr, Devon M., Beyer, Ross A., Howard, Alan D., 2012. Inverted fluvial features in the Aeolis-Zephyria Plana, western Medusae Fossae Formation, Mars: Evidence for post-formation modification. J. Geogr. Reg. Planets 117 (E3).

Lefort, Alexandra, Burr, Devon M., Nimmo, Francis, Jacobsen, Robert E., 2015. Channel slope reversal near the Martian dichotomy boundary: testing tectonic hypotheses. Geomorphology 240, 121–136.

Levy, Joseph S., Fountain, Andrew G., O'Connor, Jim E., Welch, Kathy A., Berry Lyons, W., 2013. Garwood valley, Antarctica: a new record of last glacial maximum to holocene glaciofluvial processes in the McMurdo dry valleys. Geol. Soc. Am. Bull. 125 (9–10), 1484–1502.

Lewis, Kevin W., Aharonson, Oded, 2006. Stratigraphic analysis of the distributary fan in Eberswalde crater using stereo imagery. J. Geogr. Reg. Planets 111 (E6).

Lewis, Kevin W., Aharonson, Oded, 2014. Occurrence and origin of rhythmic sedimentary rocks on Mars. J. Geogr. Reg. Planets 119 (6), 1432–1457.

Lonergan, L., Cartwright, J., Jolly, R., May 1998. The geometry of polygonal fault systems in Tertiary mudrocks of the North Sea. J. Struct. Geol. 20, 529–548. https://doi.org/10.1016/S0191-8141(97)00113-2.

Mahanti, P., Robinson, M.S., Humm, D.C., Stopar, J.D., 2014. A standardized approach for quantitative characterization of impact crater topography. Icarus 241, 114–129.

Malin, M.C., Edgett, K.S., December 2000. Sedimentary rocks of early Mars. Science 290, 1927–1937. https://doi.org/10.1126/science.290.5498.1927.

Mangold, N., 2011. Water ice sublimation-related landforms on Mars. Geol. Soc. Lond. Special Publ. 356 (1), 133–149.

Melosh, H. Jay, 2011. Planetary Surface Processes, vol. 13. Cambridge University Press.

Mouginis-Mark, Peter J., Boyce, Joseph M., 2012. Tooting crater: geology and geomorphology of the archetype large, fresh, impact crater on Mars. Chemie der Erde - Geochem. 72 (1), 1–23. ISSN 0009-2819. https://doi.org/10.1016/j.chemer.2011.12.001. http://www.sciencedirect.com/science/article/pii/S0009281911000882.

Nachon, M., Clegg, S.M., Mangold, N., Schröder, S., Kah, L.C., Dromart, G., Ollila, A., Johnson, J.R., Oehler, D.Z., Bridges, J.C., et al., 2014. Calcium sulfate veins characterized by ChemCam/Curiosity at Gale crater, Mars. J. Geogr. Reg. Planets 119 (9), 1991–2016. https://doi.org/10.1002/2013JE004588. ISSN 2169-9100.

Odonne, Francis, Ménard, Isabelle, Massonnat, Gérard J., Rolando, Jean-Paul, 1999. Abnormal reverse faulting above a depleting reservoir. Geology 27 (2), 111–114.

Okubo, Chris H., Lewis, Kevin W., McEwen, Alfred S., Kirk, Randolph L., 2008. Relative age of interior layered deposits in southwest Candor Chasma based on high-resolution structural mapping. J. Geogr. Reg. Planets 113 (E12).

Palucis, M.C., Dietrich, W.E., Williams, R.M.E., Hayes, A.G., Parker, T., Sumner, D.Y., Mangold, N., Lewis, K., Newsom, H., March 2016. Sequence and relative timing of large lakes in Gale crater (Mars) after the formation of Mount Sharp. J. Geogr. Reg. Planets 121, 472–496. https://doi.org/10.1002/2015JE004905.

Palucis, Marisa Christina, 2014. Using Quantitative Topographic Analysis to Understand the Role of Water on Transport and Deposition Processes on Crater Walls. PhD thesis. UC Berkeley.

Panda, B.B., Rucker, M.L., Fergason, K.C., 2015. Modeling of earth fissures caused by land subsidence due to groundwater withdrawal. Proc. Int. Assoc. Hydrol. Sci. 372, 69.

Parteli, Eric J.R., Durán, Orencio, Tsoar, Haim, Schwämmle, Veit, Herrmann, Hans J., 2009. Dune formation under bimodal winds. Proc. Natl. Acad. Sci. Unit. States Am. 106 (52), 22085–22089.

Rapin, W., Meslin, P.-Y., Maurice, S., Vaniman, D., Nachon, M., Mangold, N., Schröder, S., Gasnault, O., Forni, O., Wiens, R.C., Martínez, G.M., Cousin, A., Sautter, V., Lasue, J., Rampe, E.B., Archer, D., October 2016. Hydration state of calcium sulfates in Gale crater, Mars: identification of bassanite veins. Earth Planet Sci. Lett. 452, 197–205. https://doi.org/10.1016/j.epsl.2016.07.045.

Sclater, John G., Christie, P.A.F., 1980. Continental stretching; an explanation of the post-Mid-Cretaceous subsidence of the central North Sea basin. J. Geophys. Res. 85 (B7), 3711–3739.

Stack, K.M., Grotzinger, J.P., Milliken, R.E., 2013. Bed thickness distributions on Mars: an orbital perspective. J. Geogr. Reg. Planets 118 (6), 1323–1349.

Tanaka, K.L., Robbins, S.J., Fortezzo, C.M., Skinner, J.A., Hare, T.M., 2014. The digital global geologic map of Mars: chronostratigraphic ages, topographic and crater morphologic characteristics, and updated resurfacing history. Planet. Space Sci. 95, 11–24.

Tornabene, L.L., Ling, V., Osinski, G.R., Boyce, J.M., Harrison, T.N., McEwen, A.S., March 2013. A revised global depth-diameter scaling relationship for Mars based on pitted impact melt-bearing craters. In: Lunar and Planetary Science Conference, vol. 44, p. 2592.

Wangen, Magnus, 2010. Physical Principles of Sedimentary Basin Analysis. Cambridge University Press.

Williams, R.M.E., Weitz, C.M., November 2014. Reconstructing the aqueous history within the southwestern Melas basin, Mars: clues from stratigraphic and morphometric analyses of fans. Icarus 242, 19–37. https://doi.org/10.1016/j.icarus.2014.06.030.

Williams, Rebecca M.E., Irwin, Rossman P., Burr, Devon M., Harrison, Tanya, McClelland, Phillip, 2013. Variability in martian sinuous ridge form: Case study of Aeolis Serpens in the Aeolis Dorsa, Mars, and insight from the Mirackina paleoriver, South Australia. Icarus 225 (1), 308–324.

Zabrusky, K., Andrews-Hanna, J.C., Wiseman, S.M., August 2012. Reconstructing the distribution and depositional history of the sedimentary deposits of Arabia Terra, Mars. Icarus 220, 311–330.